
The Error of Deep Operator Networks Is the Sum of Its Parts: Branch-Trunk and Mode Error Decompositions

Alexander Heinlein

Delft Institute of Applied Mathematics
Delft University of Technology
Delft, 2628CD, The Netherlands
a.heinlein@tudelft.nl

Johannes Taraz

Delft Institute of Applied Mathematics
Delft University of Technology
Delft, 2628CD, The Netherlands
johannes.taraz@gmail.com

Abstract

Operator learning has the potential to strongly impact scientific computing by learning solution operators for differential equations, potentially accelerating multi-query tasks such as design optimization and uncertainty quantification by orders of magnitude. Despite proven universal approximation properties, deep operator networks (DeepONets) often exhibit limited accuracy and generalization in practice, which hinders their adoption. Understanding these limitations is therefore crucial for further advancing the approach.

This work analyzes performance limitations of the classical DeepONet architecture. It is shown that the approximation error is dominated by the branch network when the internal dimension is sufficiently large, and that the learned trunk basis can often be replaced by classical basis functions without a significant impact on performance.

To investigate this further, a modified DeepONet is constructed in which the trunk network is replaced by the left singular vectors of the training solution matrix. This modification yields several key insights. First, a spectral bias in the branch network is observed, with coefficients of dominant, low-frequency modes learned more effectively. Second, due to singular-value scaling of the branch coefficients, the overall branch error is dominated by modes with intermediate singular values rather than the smallest ones. Third, using a shared branch network for all mode coefficients, as in the standard architecture, improves generalization of small modes compared to a stacked architecture in which coefficients are computed separately. Finally, strong and detrimental coupling between modes in parameter space is identified.

1 Introduction

Operator learning Many systems in science and engineering can be formulated using differential equations, and a large body of research exists on solving them efficiently and accurately.

This work focuses on approximating the time evolution operator of time-dependent partial differential equations (PDEs), which maps the initial condition to the solution at a later time. Classical numerical methods (e.g., finite elements with time-stepping) efficiently compute solutions for individual initial conditions but offer no efficient way to approximate the entire operator, as each initial condition requires repeated integration.

Approximating solution operators is crucial for tasks such as PDE-constrained optimization [1, 2] and uncertainty quantification [3]. Operator learning (OL) methods directly approximate mappings between function spaces using neural networks [4, 5, 6], complementing classical reduced order modeling (ROM) [7, 8]. OL is central to scientific machine learning, combining techniques from scientific computing and machine learning [9].

Deep operator networks (DeepONets) Building on theoretical results by Chen and Chen [10], Lu et al. [4] introduced DeepONets, which have become a standard architecture for operator learning. The DeepONet consists of two sub-networks: the trunk network outputs N basis functions evaluated at coordinate x , and the branch network

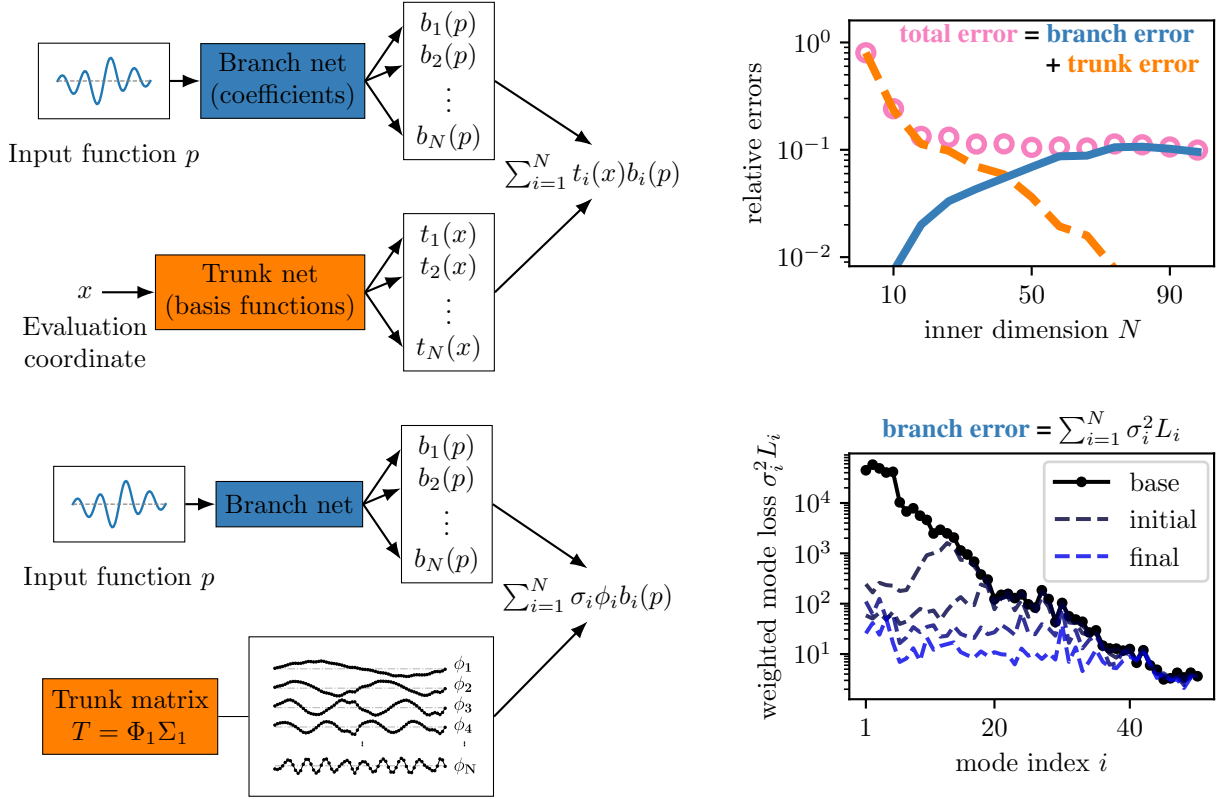


Figure 1: Visualizations of the standard DeepONet (top left) and this work’s main contributions: the decomposition into trunk and branch error (top right) and the modified DeepONet’s architecture (bottom left) which allows us to further investigate the dominant branch error via the mode loss decomposition (bottom right). The visualizations of the architectures are adapted and reproduced from [4].

outputs coefficients for these basis functions given a sampled initial condition. The output is a linear combination of trunk basis functions with branch coefficients. The architecture is visualized in fig. 1 (top left). Despite theoretical guarantees, DeepONets face practical limitations including high training data demands and limited generalizability. Various modifications have been proposed; for a comprehensive overview see [11]. Some notable modifications are Kolmogorov-Arnold-DeepONets [12], improved architectures [13], two-step training with trunk orthogonalization [14], and multi-fidelity training [15, 16, 17].

Other operator learning approaches Other OL approaches include learning Green’s functions for interpretable solutions of linear PDEs [18, 19, 20, 21], and addressing resolution dependence through Fourier neural operators [22, 5], convolutional neural operators [6, 23, 24], and Laplace neural operators [25]. Additionally, there are theoretical investigations of errors [26, 27, 14, 28] in DeepONets and other neural operator architectures. Physics-informed neural networks (PINNs) [29, 30, 31] form another pillar of scientific ML, and can be combined with DeepONets [32, 33, 34, 35, 36, 37, 38].

Related work Our work is inspired by the theoretical work by Lanthaler et al. [27] analyzing DeepONet error. Moreover, in section 6, we use a modified DeepONet: the trunk network is replaced by fixed basis vectors derived from the singular value decomposition (SVD) of the training data matrix, as this basis captures most of the variance in the data. This is (up to a scaling with the singular values and a whitening of the data) very similar to the POD-DeepONet [39] and the SVD-DeepONet [40]. In addition, the fixed basis functions studied in section 5 are similar to the spectral neural operator [41], and fixed bases (for input and output) are also used in the principal component analysis (PCA) neural operator [3, 42]. Beyond PCA, using the bases from nonlinear methods, such as kernel-PCA, for OL has been investigated in [43]. A direct comparison between DeepONets and ROM and their combination has been studied in [44], by training a DeepONet to learn the residual of a classical ROM. Related to our study of the

DeepONet’s projection error is the investigation of the basis functions learned by a DeepONet and their use for a spectral method in [45]. In this work, we also investigate spectral bias [46], i.e., the tendency of neural networks to learn low-frequency components faster than high-frequency ones. While previous works, such as [47, 48, 49, 50, 51], examine spectral bias in the spatial dependency, our investigation focuses on spectral bias in the branch network, which captures the input function dependency. Additionally, by comparing the unstacked and stacked DeepONets [4] (i.e., the architectural coupling of the modes), we establish a connection to the field of multi-task learning (MTL) [52]. Lastly, just as we exploit the specific DeepONet structure to decompose the error and gain insight into the network’s inner workings, [53] leverage this same structure to develop a more efficient optimization algorithm.

Outline Section 3 describes the DeepONet architecture, training/testing setup, and data. In section 4, we decompose the error into trunk and branch components. Section 5 investigates the trunk network by replacing learned basis functions with fixed bases, showing that branch error dominates for large N (cf. fig. 1 (top right)). In section 6, we modify the DeepONet with a fixed SVD basis, enabling mode loss decomposition. We find that intermediate modes contribute significantly to branch error (cf. fig. 1 (bottom right)) and observe spectral bias in the branch network for advection-diffusion, KdV, and Burgers’ equations. This reveals, on the one hand, the improved generalization through parameter sharing, and on the other hand, the detrimental coupling between modes in DeepONets trained with gradient descent. Furthermore, Adam mitigates gradient imbalance across singular value scales. Section 7 concludes with discussion and limitations. Table 1 contains notation. To summarize, our three main contributions are:

1. We systematically study trunk and branch errors with respect to the inner dimension N for practical examples.
2. We decompose the branch error into modes, showing significant contributions of the intermediate modes.
3. The decomposition enables analysis of spectral bias in the branch network and mode coupling effects.

The code and data from this study are available at <https://github.com/jotaraz/ModeDecomposition-DeepONets>.

2 Glossary

symbol	name	note	
Z^+	Moore–Penrose inverse of matrix Z		
$\text{ran}(Z)$	range / column space of matrix Z		
$\ Z\ _F$	Frobenius norm	$\ Z\ _F := \sqrt{\sum_{ij} Z_{ij}^2}$	
N	number of output neurons of branch and trunk net (“inner dimension”)	$N \in \mathbb{N}$	eq. (3)
\mathcal{X}	spatial domain of interest	$\mathcal{X} \subset \mathbb{R}^d$	sec. 3.2
$\mathcal{C}(\mathcal{X})$	set of continuous functions on \mathcal{X}		
u	solution function of time-dependent PDE	$u \in \mathcal{C}(\mathcal{X} \times [0, \tau])$	sec. 3.2
p	input function (e.g., initial condition of time-dependent PDE), later also used for discretized input function	$p(\cdot) = u(\cdot, t = 0) \in \mathcal{C}(\mathcal{X})$	sec. 3.2
τ	evolution time	$p(\cdot) \mapsto u(\cdot, \tau)$	sec. 3.2
m	number of input functions in a data set	$m \in \mathbb{N}$	sec. 3.4
M	number of sampling points of p	$M \in \mathbb{N}$	sec. 3.3
\bar{x}_j	j -th sampling point of p with $1 \leq j \leq M$	$\bar{x}_j \in \mathcal{X}$	sec. 3.3
\hat{p}	discretized input function (sampled at \bar{x}_j), later p is used to denote this too	$\hat{p} \in \mathbb{R}^M$	sec. 3.3
G	true solution operator	$G : p(\cdot) \mapsto u(\cdot, t = \tau)$	sec. 3.2
\tilde{G}_θ	approximation of G (using a DeepONet)		sec. 3.2
x	coordinate at which $G(p)(\cdot)$ and $\tilde{G}_\theta(\hat{p})(\cdot)$ are evaluated	$x \in \mathcal{X}$	
n	number of coordinates to evaluate $G(p)(\cdot)$ and $\tilde{G}_\theta(\hat{p})(\cdot)$ in test and training data	$n \in \mathbb{N}$	sec. 3.4
A	target data matrix	$A \in \mathbb{R}^{n \times m}$	sec. 3.4
t_k	k -th trunk output neuron: either a function $t_k(x)$ or a vector $t_k = (t_k(x_1) \dots t_k(x_n))^T$	$t_k \in \mathcal{C}(\mathcal{X})$ or $t_k \in \mathbb{R}^n$	sec. 3.3
T	trunk output matrix	$T_{ik} = t_k(x_i), T \in \mathbb{R}^{n \times N}$	sec. 3.4

b_k	k -th branch output neuron: either a function $b_k(p)$ or a vector $b_k = (b_k(p_1) \dots b_k(p_m))^T$	$\bar{b}_k \in \mathcal{C}(\mathbb{R}^M)$ or $b_k \in \mathbb{R}^m$	sec. 3.3
B	branch output matrix	$B_{jk} = b_k(p_j), B \in \mathbb{R}^{m \times N}$	sec. 3.4
\tilde{A}	approximation of A by the DeepONet	$\tilde{A} = TB^T \in \mathbb{R}^{n \times m}$	sec. 3.4
ε	squared total error of DeepONet approximation	$\varepsilon := \ A - \tilde{A}\ _F^2$	sec. 4.2
δ	relative error of DeepONet approximation	$\delta := \sqrt{\varepsilon}/\ A\ _F$	
X_{tr}	training variant of a variable X (e.g., $X = \varepsilon, A, \dots$)		
X_{te}	test variant of a variable X		
σ_k	k -th singular value of A_{tr} (ordered descendingly)	$\Sigma = \text{diag}(\sigma_1, \dots, \sigma_r)$	eq. (5)
ϕ_k	k -th mode / k -th left singular vector of A_{tr}	$\phi_k \in \mathbb{R}^n, \Phi = [\phi_1 \dots \phi_r]$	eq. (5)
v_k	optimal coefficients for the k -th mode and the training data's input functions / k -th right singular vector of A_{tr}	$v_k \in \mathbb{R}^{m_{tr}}, V = [v_1 \dots v_r]$	eq. (5)
w_k	optimal coefficients for the k -th mode and the test data's input functions	$w_k \in \mathbb{R}^{m_{te}}$	
\mathcal{L}	loss / mean-squared error of DeepONet approximation	$\varepsilon/(nm)$	
$L_{k,tr}$	unweighted training loss of mode k	$\ b_{k,tr} - v_k\ _2^2$	eq. (8)
$L_{k,te}$	unweighted test loss of mode k (normalized for comparability to $L_{k,tr}$)	$\frac{m_{tr}}{m_{te}} \ b_{k,te} - w_k\ _2^2$	eq. (9)
$\sigma_k^2 L_k$	weighted loss of mode k		sec. 6.2
–	unweighted base loss / mode loss L_k for $b_k = 0$	1 (train), $\frac{m_{tr}}{m_{te}} \ w_k\ _2^2$ (test)	sec. 6.2
–	weighted base loss / mode loss $\sigma_k^2 L_k$ for $b_k = 0$	σ_k^2 (train), $\sigma_k^2 \frac{m_{tr}}{m_{te}} \ w_k\ _2^2$ (test)	sec. 6.2

Table 1: Notation frequently used in this work.

3 Background and Setup

This section provides background on neural networks, the problem setup (time evolution under a PDE), the DeepONet architecture, and the training/testing framework.

3.1 Foundations of Neural Networks and Machine Learning

This section provides a self-contained overview of foundational concepts in neural networks and optimization algorithms used to train them. Consider approximating a function f using a parametric model \tilde{f}_θ with parameters θ . Given inputs $\{x_1, \dots, x_m\}$ and target outputs $\{y_1, \dots, y_m\}$ with $y_i = f(x_i)$, training finds optimal parameters

$$\theta_{opt} \in \arg \min_{\theta} \sum_{i=1}^m |y_i - \tilde{f}_\theta(x_i)|^2,$$

minimizing the mean-squared error (training loss)

$$\mathcal{L}_{tr}(\theta) = \frac{1}{m} \sum_{i=1}^m |y_i - \tilde{f}_\theta(x_i)|^2. \quad (1)$$

3.1.1 Neural Networks

By the universal approximation theorem [54, 55], neural networks can approximate continuous functions. A one-layer network models

$$\tilde{f}_\theta(x) = \sum_{k=1}^N \theta_k^{(out)} \sigma \left(\left(\vartheta_k^{(W,1)} \right)^T x + \vartheta_k^{(B,1)} \right) = \theta^{(out)} H_{\theta^{(1)}}(x),$$

where $H_{\theta^{(1)}}(x) := \sigma \left(\left(\vartheta^{(W,1)} \right)^T x + \vartheta^{(B,1)} \right)$ is the hidden layer with parameters $\theta^{(1)} = (\vartheta^{(W,1)}, \vartheta^{(B,1)})$, and σ is a non-polynomial activation function. Each term $\sigma \left(\left(\vartheta_k^{(W,1)} \right)^T x + \vartheta_k^{(B,1)} \right)$ in this sum is called a *neuron*. Multi-layer perceptrons (MLPs) apply D hidden layers successively: $z_1 = H_{\theta^{(1)}}(x)$, $z_2 = H_{\theta^{(2)}}(z_1)$, etc., with output

$\tilde{f}_\theta(x) = \theta^{(out)} z_D$. The parameters are

$$\theta = \left(\theta^{(1)}, \theta^{(2)}, \dots, \theta^{(D)}, \theta^{(out)} \right). \quad (2)$$

This composition is done because, in practice, it reduces the number of necessary parameters for a given accuracy [56], compared with a perceptron with a single hidden layer. The number of hidden layers D is called depth, hence the term *deep learning* for neural networks with multiple hidden layers. The number of neurons in one layer is often called the *width* of this layer. If all layers have the same width, this is referred to as the neural network's *hidden layer width* w .

We use GELU activation [57]: $\sigma(x) = GELU(x) := \frac{x}{2} \left(1 + \operatorname{erf} \left(\frac{x}{\sqrt{2}} \right) \right)$.

3.1.2 Optimization Schemes

Gradient descent (GD) updates parameters θ_t iteratively: $\theta_{t+1} = \theta_t - \alpha_t \nabla \mathcal{L}_{tr}(\theta_t)$, where α_t is the learning rate [58, 59]. However, GD often converges slowly or gets trapped in local minima. Adam [60] combines momentum [61] and adaptive learning rates [62, 63]. The update $\theta_{t+1} = \theta_t + \delta\theta_t$ uses:

$$\begin{aligned} m_t &= \beta_1 m_{t-1} + (1 - \beta_1) \nabla \mathcal{L}_{tr}(\theta_t), & v_t &= \beta_2 v_{t-1} + (1 - \beta_2) (\nabla \mathcal{L}_{tr}(\theta_t))^2, \\ \hat{m}_t &= \frac{m_t}{1 - \beta_1^t}, & \hat{v}_t &= \frac{v_t}{1 - \beta_2^t}, \\ \delta\theta_t &= -\alpha_t \frac{\hat{m}_t}{\sqrt{\hat{v}_t + \bar{\epsilon} + \epsilon}}. \end{aligned}$$

The learning rate α_t may follow a schedule (e.g., constant or exponential decay). Unless stated otherwise, we use Adam. Hyperparameters are listed in section A.

3.2 General Problem Setup

Consider the time-dependent PDE on spatial domain $\mathcal{X} \subset \mathbb{R}^d$ and time interval $(0, \tau]$:

$$\begin{aligned} \frac{\partial u}{\partial t} &= \mathcal{D}(u), & \text{in } \mathcal{X} \times (0, \tau], \\ \mathcal{B}(u) &= 0, & \text{on } \partial\mathcal{X} \times (0, \tau], \\ u(\cdot, 0) &= p(\cdot), & \text{in } \mathcal{X}, \end{aligned}$$

where \mathcal{D} is a (possibly nonlinear) differential operator, \mathcal{B} denotes a suitable boundary condition on $\partial\mathcal{X}$, and $p \in \mathcal{C}(\mathcal{X})$ is the initial condition. Under appropriate regularity assumptions on \mathcal{X} , \mathcal{D} , \mathcal{B} , and p , this PDE admits a unique solution $u \in \mathcal{C}(\mathcal{X} \times [0, \tau])$. We then define the time evolution (or solution) operator

$$G : \mathcal{C}(\mathcal{X}) \rightarrow \mathcal{C}(\mathcal{X}), \quad p(\cdot) \mapsto u(\cdot, \tau),$$

which maps the initial condition to the solution at time τ .

Remark 1. The function p plays multiple roles: it is the initial condition of the PDE, the input to the solution operator G , and the function that parametrizes the solution. Correspondingly, the operator learning literature uses the terms initial condition, input function, and parameter function interchangeably. We adopt input function throughout this work.

3.3 DeepONet

The DeepONet, as introduced in [4], is designed to approximate such solution operators. It can be seen as a deep neural network realization of the architecture in the generalized universal approximation theorem for operators in [10]. To make the infinite dimensional problem, that is, mapping $p(\cdot) \in \mathcal{C}(\mathcal{X})$ to $u(\cdot, \tau) \in \mathcal{C}(\mathcal{X})$, computationally accessible, the initial condition p is encoded in a finite dimensional vector space as $\hat{p} = (p(\bar{x}_1) \dots p(\bar{x}_M))^T \in \mathbb{R}^M$ by sampling at M locations. This potentially involves a loss of information, which we will also address in section 3.4. As mentioned briefly before, the DeepONet is a neural network consisting of two sub-networks: the trunk network outputs $t_k(x)$ given coordinate x , and the branch network outputs $b_k(\hat{p})$ given \hat{p} . The final output is

$$\tilde{G}_\theta(\hat{p})(x) = \sum_{k=1}^N b_k(\hat{p}) t_k(x), \quad (3)$$

where θ are parameters and N is the number of output neurons of both trunk and branch network; see also fig. 1 (top left). Equivalently, the DeepONet’s output is a linear combination of the N trunk output neurons $t_k(x)$ with the branch network’s output neurons $b_k(\hat{p})$ as coefficients. Thus, all DeepONet output functions $\tilde{G}_\theta(\hat{p})(\cdot)$ lie in the *trunk space* $\mathcal{T}(N) := \text{span}\{t_k\}_{k=1}^N \subset \mathcal{C}(\mathcal{X})$. The dimension of $\mathcal{T}(N)$ is at most N , with equality when the trunk functions $\{t_k\}_{k=1}^N$ are linearly independent; in practice, this is typically the case. For simplicity, we call N the *inner dimension of the DeepONet* and we denote the trunk functions as basis functions.

Both trunk and branch network are usually implemented as MLPs, but other choices are possible, as previously mentioned. We focus on this standard architecture with MLP-based designs; analyzing more advanced DeepONet variants is left to future work. The parameters of both sub-networks together form θ , the DeepONet’s parameters. These are found by minimizing the mean-squared loss

$$\mathcal{L}(\theta) = \frac{1}{K} \sum_{i=1}^K |G(p_i)(x_i) - \tilde{G}_\theta(\hat{p}_i)(x_i)|^2,$$

over K samples of input functions p_i and evaluation coordinates x_i .

3.4 Setup for Training and Testing

Our setup uses:

1. Initial conditions from a low-dimensional subspace with sufficient sampling (M large) such that p is reconstructible from \hat{p} . For simplicity, we thus stop distinguishing between p and \hat{p} (details in section B).
2. Discretization with m initial conditions $(p_j)_{j=1,\dots,m}$ and n evaluation coordinates $(x_i)_{i=1,\dots,n}$, yielding $K = nm$ training points, i.e., the full tensor product of these discretizations.
3. Same evaluation coordinates for training and testing ($n_{tr} = n_{te} = n$), focusing on generalization in parameter space.

We arrange the targets (or true solutions) in a matrix $A_{ij} = G(p_j)(x_i)$, such that $A \in \mathbb{R}^{n \times m}$. The DeepONet output is

$$\tilde{A}_{ij} = \tilde{G}_\theta(p_j)(x_i) = \sum_{k=1}^N t_k(x_i) b_k(p_j) \iff \tilde{A} = TB^T,$$

where $T_{ik} = t_k(x_i) \in \mathbb{R}^{n \times N}$ and $B_{jk} = b_k(p_j) \in \mathbb{R}^{m \times N}$ are trunk and branch outputs. The loss is $\mathcal{L}(\theta) = \frac{1}{K} \|A - \tilde{A}\|_F^2$ with Frobenius norm $\|Z\|_F^2 = \sum_{ij} z_{ij}^2$. This matrix notation simplifies analysis and enables efficient computation by evaluating T once for all inputs.

3.5 Data and Experiments

In this work, we train DeepONets to approximate the time evolution operators that map the initial condition to the solution at a given final time τ . Our standard example problem is the KdV equation, similar to [45],

$$\begin{aligned} 0 &= \frac{\partial u}{\partial t} + \frac{u}{2\pi} \frac{\partial u}{\partial x} + \frac{0.01}{8\pi^3} \frac{\partial^3 u}{\partial x^3} & \forall x \in (0, 1), t > 0, & \frac{\partial^2 u}{\partial x^2}(0, t) = \frac{\partial^2 u}{\partial x^2}(1, t) & \forall t \geq 0, \\ u(0, t) = u(1, t) & \forall t \geq 0, & u(x, t = 0) = p(x) & \forall x \in (0, 1), \\ \frac{\partial u}{\partial x}(0, t) = \frac{\partial u}{\partial x}(1, t) & \forall t \geq 0, & p(x) = \sum_{k=1}^5 a_k \sin(2\pi kx) & \forall x \in (0, 1), \end{aligned}$$

with $\tau = 0.2$. Most results shown in this work are computed for this standard example. We also consider the advection-diffusion equation and Burgers’ equation, training separate operators for each PDE and value of τ . Unless stated otherwise, the observations reported apply qualitatively to all example problems described in section C; in general, we report results only for the KdV equation and include additional examples when they offer new insights or qualitative differences.

4 Error Decomposition Into Trunk and Branch Errors

In this section, we define the projection error and formalize how the total approximation error is distributed between trunk and branch. As mentioned in section 3.4, we consider a fixed evaluation grid for the trunk network as this simplifies the further discussion. Thus, we now use the terms basis functions and basis vectors (obtained through the evaluation of the basis functions on the grid) interchangeably.

4.1 Projection Error

Consider a set of vectors $\{a_i\}_{i=1}^m \subset \mathbb{R}^n$ and a basis $\{t_k\}_{k=1}^N \subset \mathbb{R}^n$. The error of projecting $\{a_i\}_{i=1}^m$ onto the space spanned by $\{t_k\}_{k=1}^N \subset \mathbb{R}^n$, or the *projection error*, quantifies how well the a_i can be reconstructed through optimal linear combinations of the t_k . For accurate reconstruction, this error should be small. More formally, we define the projection error as

$$\varepsilon_P(T, A) := \|(I - TT^+)A\|_F^2,$$

where $T = [t_1 \dots t_N] \in \mathbb{R}^{n \times N}$, $A = [a_1 \dots a_m] \in \mathbb{R}^{n \times m}$, and T^+ denotes the Moore-Penrose inverse of T . Here, TT^+ represents the orthogonal projection onto the span of the $\{t_k\}_{k=1}^N$. Thus, $(I - TT^+)A$ captures the part of A that cannot be represented by the t_k [64].

4.2 Trunk and Branch Errors

We adapt the error decomposition framework of Lanthaler et al. [27] with two simplifications: we eliminate the encoding error by ensuring p can be reconstructed from \hat{p} (cf. section 3.4), and we define the error over a finite sample set rather than a probability measure over the input space. This allows for a more direct analysis of how the total approximation error splits between trunk and branch networks. We consider the difference between the DeepONet's output \tilde{A} and the target data matrix A :

$$\tilde{A} - A = TB^T - A = TB^T - TT^+A + TT^+A - A = T(B^T - T^+A) + (TT^+ - I)A.$$

Since $T(B^T - T^+A)$ and $(TT^+ - I)A$ are orthogonal to each other, this yields the error decomposition

$$\varepsilon := \|\tilde{A} - A\|_F^2 = \underbrace{\|T(B^T - T^+A)\|_F^2}_{=: \varepsilon_B} + \underbrace{\|(TT^+ - I)A\|_F^2}_{=: \varepsilon_T = \varepsilon_P(T, A)}. \quad (4)$$

In the following sections, we investigate the different error components ε_B and ε_T .

4.2.1 Trunk Error

Equation (4) thus defines the trunk error ε_T as the projection error $\varepsilon_P(T, A)$ with the trunk matrix T , that is, the error of projecting the target data matrix onto the trunk space, cf. section 3.3. This formally proves that a small projection error is necessary for a small error ε , but in general, not sufficient. Now, we consider the SVD of the training data matrix

$$A = \Phi \Sigma V^T = [\Phi_1 \Phi_2] \begin{bmatrix} \Sigma_1 & 0 \\ 0 & \Sigma_2 \end{bmatrix} \begin{bmatrix} V_1^T \\ V_2^T \end{bmatrix} = \Phi_1 \Sigma_1 V_1^T + \Phi_2 \Sigma_2 V_2^T, \quad (5)$$

with $\Phi_1 \in \mathbb{R}^{n \times N}$, $\Sigma_1 \in \mathbb{R}^{N \times N}$ and $V_1 \in \mathbb{R}^{m \times N}$. Then, the Eckart-Young-Mirsky theorem [65] states that the projection error for all matrices $T \in \mathbb{R}^{n \times N}$ satisfies $\varepsilon_P(T, A) \geq \|\Sigma_2\|_F^2$, with equality achieved by $T = \Phi_1 C$ for any full-rank matrix $C \in \mathbb{R}^{N \times N}$. Intuitively, this is because the first N left singular vectors of A capture the N principal directions of A , that is, the N directions with the highest variance.

4.2.2 Branch Error

To better understand the branch error ε_B , we first compute the branch matrix B_* , which is optimal in the following sense: given a trunk matrix T , B_* is the branch matrix for which TB^T best approximates A in the Frobenius norm.

$$\begin{aligned} B_* &= \arg \min_{B \in \mathbb{R}^{m \times N}} \|A - TB^T\|_F^2 = \arg \min_{B \in \mathbb{R}^{m \times N}} \|(I - TT^+)A + TT^+A - TB^T\|_F^2 \\ &= \arg \min_{B \in \mathbb{R}^{m \times N}} (\|(I - TT^+)A\|_F^2 + \|T(T^+A - B^T)\|_F^2) = \arg \min_{B \in \mathbb{R}^{m \times N}} \|T(T^+A - B^T)\|_F^2 = (T^+A)^T. \end{aligned}$$

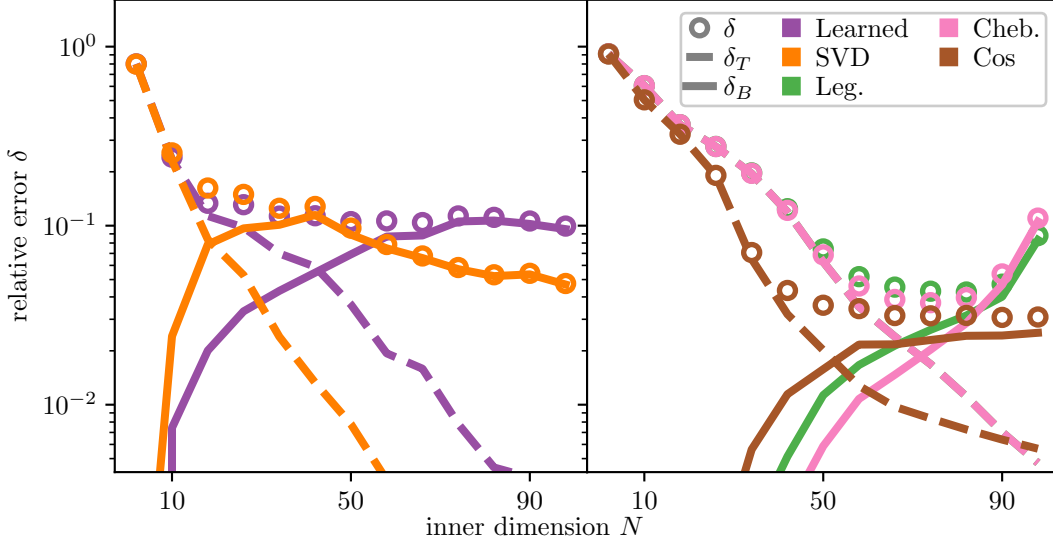


Figure 2: **Relative total, trunk and branch errors of DeepONets with various bases plotted over N .** Colors: Purple lines: learned trunk (standard DeepONet), orange: SVD basis, green: Legendre polynomials, pink: Chebyshev polynomials, brown: cosine. Line-symbols: Total error δ (circle), trunk error δ_T (dashed), branch error δ_B (solid). The relative error is defined in the glossary, table 1.

Thus, when investigating the branch network, one might intuitively define the branch error as

$$\varepsilon_C := \|B - B_*\|_F^2 = \|B - (T^+ A)^T\|_F^2 = \|B^T - T^+ A\|_F^2, \quad (6)$$

that is, the difference between the actual branch matrix B and the optimal branch matrix B_* . The inequality

$$\varepsilon \leq \|T\|_2^2 \underbrace{\|B^T - T^+ A\|_F^2}_{\varepsilon_C} + \|(TT^+ - I)A\|_F^2 \quad (7)$$

can be derived as a bound on ε . While ε_C puts the same weight on the error of each branch neuron, $\varepsilon_B = \|T(B^T - T^+ A)\|_F^2$ accounts for the trunk matrix T , weighting the approximation error of each branch neuron (column of B) by the norm of the corresponding trunk neuron. Hence, we use ε_B as the branch error.

Remark 2. In practice, eq. (7) is a very loose bound, since the norms of the trunk neurons vary strongly, cf. section D.

5 Investigating the Trunk Network

The error decomposition enables systematic investigation of the trunk network. Many trunk modifications exist: orthogonalization [14], Fourier features [39], SVD basis [3, 39], Chebyshev or trigonometric functions [41], and transfer learning [45]. We investigate: (1) How do prescribed bases compare to learned bases? (2) Does the learned trunk approach optimal trunk error? (3) How is the error distributed between trunk and branch?

We compare different bases t_k , either learned or prescribed, but the output remains $\sum_{k=1}^N t_k(x)b_k(p)$. We test (details in section E): Learned (standard DeepONet), SVD (t_k is k -th left singular vector of A), Legendre (k -th Legendre polynomial), Chebyshev (k -th Chebyshev polynomial), Cosine ($t_k(x) = \cos((k-1)\pi x)$).

Figure 2 shows errors for different bases. For small N , learned and SVD bases perform best. The learned basis plateaus around $N = 20$, while SVD error decreases slowly. Legendre and Chebyshev errors decrease until $N = 70$, then increase. For large N , cosine achieves lowest total error. Across examples, all bases match or exceed learned basis performance for large N .

The SVD basis achieves the lowest trunk error on training data by the Eckart-Young-Mirsky theorem [65]. Figure 2 shows empirically that this translates to the test data as well (see section G for further discussion). However, optimal projection error doesn't guarantee optimal total error – low branch error is also necessary. For large N , trunk errors become negligible for all bases. This implies, in particular, that the standard DeepONet learns trunk functions spanning the solutions.

The non-negligible total error for large N implies significant branch error, which increases with N . For Legendre and Chebyshev, this causes total error to increase. Intuitively, approximating 10 coefficients is easier than 90. Motivated by this, we study branch errors in detail next.

6 Investigating the Branch Network

In section 5, we observed that, for our examples and large N , the branch error dominates (i.e., the coefficient approximation is poor). In this section, we study whether all coefficients are poorly approximated or only those for certain basis vectors, and why. To this end, we introduce the DeepONet with the fixed SVD basis in section 6.1. In section 6.2, we decompose the branch error into individual coefficient errors, which we also refer to as mode losses. Next, in section 6.3, we analyze the distribution of the mode losses in practice. Lastly, in section 6.4, we study phenomena that affect the coefficient error distribution, such as spectral bias and inter-coefficient coupling.

6.1 Modified DeepONet

	matrix formulation	individual evaluation
true solution (train)	$(\Phi_1 \Sigma_1 V_1^T + \Phi_2 \Sigma_2 V_2^T)_{ij}$	$= \sum_{k=1}^r \sigma_k(\phi_k)_i (v_k)_j$
true solution (test)	$(\Phi_1 \Sigma_1 W_1^T + \Phi_2 \Sigma_2 W_2^T)_{ij}$	$= \sum_{k=1}^r \sigma_k(\phi_k)_i (w_k)_j$
stand. DeepONet	$(TB^T)_{ij}$	$= \sum_{k=1}^N t_k(x_i) b_k(p_j)$
mod. DeepONet	$(\Phi_1 \Sigma_1 B^T)_{ij}$	$= \sum_{k=1}^N \sigma_k(\phi_k)_i b_k(p_j)$

Table 2: Comparison of true solution (train/test), modified DeepONet and standard DeepONet in matrix formulation and for individual evaluation at coordinate x_i and initial condition p_j . The rank of the data matrix is denoted as r . For better comparison to the modified DeepONet, the SVD of the true solution is displayed.

In this section, we modify the DeepONet by replacing the trunk network by the SVD basis. This modified DeepONet is used for the remainder of the work to investigate the branch network’s error. This facilitates the analysis significantly, since it reduces the DeepONet parameters to the branch network parameters.

As discussed in section 4.2.1, for any full rank matrix C , the trunk matrix $T = \Phi_1 C$, with Φ_1 chosen as the left singular vectors, minimizes the trunk error, which we call the SVD basis. We investigate this case here, using $C = \Sigma_1$ as a scaling, which corresponds to $t_k = \sigma_k \phi_k$ for the k -th output neuron. We motivate this choice in section F.

In table 2, we compare the true solution for test and training data, the modified DeepONet, and the standard DeepONet, we show their matrix formulations (center column), and the output for individual coordinates and individual input functions (right column). This shows that the optimal branch matrix for the modified DeepONet is V_1 , i.e., the matrix containing the right singular vectors. As this will be relevant in section 6.4.1, it is important to note that this is equivalent to stating that, for the initial condition p_j , the k -th branch output neuron is trained to predict V_{jk} . The neural network architecture of the modified DeepONet is visualized in fig. 1 (bottom left).

For the sake of simplicity in notation, we use the term DeepONet to refer to the modified DeepONet (with the SVD basis scaled with the singular values) for the remainder of this work. When we use the term *standard DeepONet*, we mean a DeepONet with a learned trunk basis. Additionally, we call the left-singular vectors ϕ_i the *modes* from now on.

6.2 Mode Decomposition of the Branch Error

We decompose the (modified) DeepONet’s training error by applying eq. (4) and, using the SVD of the training data matrix A_{tr} and the resulting orthogonality, split it into trunk and branch components. The branch error, which measures the total coefficient approximation error, then further decomposes into individual mode losses, each capturing

how well a single mode’s coefficient is approximated:

$$\begin{aligned}
A_{tr} &= \Phi_1 \Sigma_1 V_1^T + \Phi_2 \Sigma_2 V_2^T \\
\varepsilon_{tr} &= \|\tilde{A}_{tr} - A_{tr}\|_F^2 = \|\Phi_1 \Sigma_1 B_{tr}^T - \Phi_1 \Sigma_1 V_1^T - \Phi_2 \Sigma_2 V_2^T\|_F^2 = \|\Phi_1 \Sigma_1 B_{tr}^T - \Phi_1 \Sigma_1 V_1^T\|_F^2 + \|\Phi_2 \Sigma_2 V_2^T\|_F^2 \\
&= \|\Sigma_1 B_{tr}^T - \Sigma_1 V_1^T\|_F^2 + \|\Sigma_2\|_F^2 = \sum_{i=1}^N \sigma_i^2 \underbrace{\|b_{i,tr} - v_i\|_2^2}_{=: L_{i,tr}} + \|\Sigma_2\|_F^2
\end{aligned} \tag{8}$$

By design, the trunk space is spanned by the first N left-singular vectors of A_{tr} , so $\varepsilon_T = \|\Sigma_2\|_F^2$. With this choice the DeepONet achieves the optimal trunk error for the training data. Since $\|\Sigma_2\|_F^2$ equals the trunk error, $\|\Sigma_1 B_{tr}^T - \Sigma_1 V_1^T\|_F^2$ is the branch error.

Equation (8) thus shows the modification’s main advantage for our analysis: the branch error decomposes into errors $\sigma_i^2 L_i$ for different modes. The *unweighted mode loss* L_i is the difference between v_i and b_i , that is, the true coefficients of mode i and the coefficients b_i predicted by the DeepONet, for all input functions. Since the unweighted mode losses L_i are scaled by the squared singular values σ_i^2 to yield the total error ε in eq. (8), we define the *weighted mode loss* as $\sigma_i^2 L_i$.

A similar error decomposition can be derived for the test data. With w_i denoting the optimal coefficients to approximate the test data using the training SVD basis (see section G for details), the test branch error decomposes as

$$\varepsilon_{B,te} = \sum_{i=1}^N \sigma_i^2 \|b_{i,te} - w_i\|_2^2.$$

To facilitate comparison between training and test mode losses, we define the test mode loss

$$L_{i,te} := \frac{m_{tr}}{m_{te}} \|b_{i,te} - w_i\|_2^2 \tag{9}$$

with a normalization factor such that both losses are scaled consistently; the precise definition is given in section G.

Remark 3. To better judge whether a mode loss is low or high, we introduce the *base loss*. We seek to define the base loss, such that observing a mode loss L_i that exceeds its base loss indicates that the branch network is neglecting mode i . To this end, the base loss of mode i is defined as the loss for $b_i = 0$, i.e., when the DeepONet predicts a zero coefficient for mode i . On the training data, the unweighted base loss is $\|v_i\|_2^2 = 1$ because V_1 is semi-orthogonal, thus the weighted base loss is σ_i^2 . For the test data, the unweighted base loss is $\frac{m_{tr}}{m_{te}} \|w_i\|_2^2 \approx 1$. Thus, the weighted base loss is $\sigma_i^2 \frac{m_{tr}}{m_{te}} \|w_i\|_2^2$. Observing a mode loss L_i that exceeds its base loss means that the model performs worse than the trivial prediction $b_i = 0$.

6.3 Distribution of Mode Losses

In this section, we investigate how training and test branch errors distribute across modes. We investigate three optimization algorithms — plain GD (section 6.3.1), loss re-weighting (section 6.3.2), and Adam (section 6.3.3) — to understand their effects on mode-specific approximation quality.

Throughout this analysis, we use the following terminology: Since the i -th mode is associated with singular value σ_i (ordered descendingly), we refer to modes with low indices as *large modes*, modes with high indices as *small modes*, and those in between as *intermediate modes*. Here, we take large modes to be $i \lesssim 10$ and small modes to be $i \gtrsim 30$; this choice is somewhat arbitrary but the motivation for it will become clearer throughout the discussion of the results.

6.3.1 Gradient Descent Training

We first examine DeepONets trained using plain GD. Figure 3 shows both the unweighted mode losses L_i and the weighted mode losses $\sigma_i^2 L_i$ for both training and test data over the course of training. The respective base losses (cf. section 6.2) are shown for reference.

An interesting pattern emerges: only the largest ≈ 10 modes show significant loss reduction below their base losses during training. This creates a characteristic error distribution in the weighted mode loss, where intermediate modes (indices 12-17 in our examples) contribute most to the total error; they are neither well-approximated like large modes nor negligible like small modes due to tiny singular values. Furthermore, the mode losses corresponding to small singular values exceed the base losses, indicating neglect through the GD optimizer. These learning dynamics are

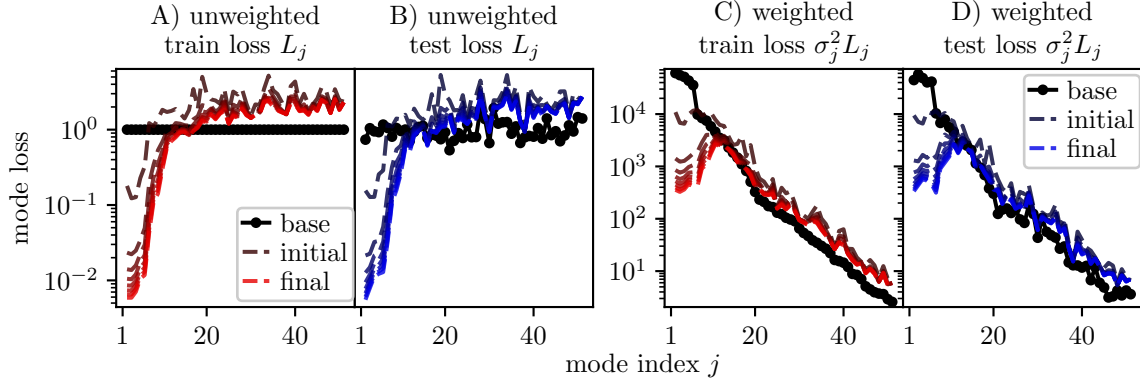


Figure 3: **Weighted mode losses for DeepONet trained with GD.** Unweighted (A,B) and weighted (C,D) training (A,C) and test (B,D) mode losses at different training stages, colored from gray (initial) to red/blue (final) shown as dashed lines. The respective base losses are shown as black dot-solid lines.

driven by gradient domination from large singular values. Since the gradient of the total loss with respect to the parameters is:

$$\nabla_{\theta} \mathcal{L} = \frac{1}{nm} \sum_{i=1}^N \sigma_i^2 \nabla_{\theta} L_i,$$

the contributions from small modes become negligible due to the σ_i^2 weighting, preventing the GD optimizer from improving their approximation even when their unweighted losses L_i are large.

Remark 4. A related phenomenon termed gradient starvation [66, 67] has been identified in classification with cross-entropy loss, where correctly classified samples cease contributing to the gradient, causing dominant features to prevent the learning of other informative features. While our setting differs (we use MSE loss where all samples continue contributing) the common thread is that gradient-based optimization can systematically neglect certain learnable components when others dominate the gradient signal.

6.3.2 Modified Loss Re-Weighting

To address the gradient imbalance, we introduce a modified loss function with adjustable mode weighting:

$$\mathcal{L}_{e,\text{tr}} = \frac{1}{nm_{\text{tr}}} \sum_{i=1}^N \sigma_i^{2+2e} L_{i,\text{tr}},$$

where the exponent e controls the re-weighting: $e < 0$ amplifies small modes, $e > 0$ emphasizes large modes, and $e = 0$ recovers the standard loss. To prevent gradient explosion or vanishing, we scale the learning rate by σ_1^{-2e} , keeping the largest mode’s contribution invariant. We use $\mathcal{L}_{e,\text{tr}}$ only to compute gradients (and thus parameter updates), not as a performance metric. Note that the re-weighted loss for $e = -1$ is equivalent to using ε_C , defined in eq. (6), instead of ε_B in the loss function.

Figure 4 shows the effect of this re-weighting. For $e = -1$, which weights all modes equally regardless of their singular values, we achieve significant loss reduction across all training modes. However, this comes with a critical trade-off: small modes improve dramatically in training but severely overfit, with test losses near base levels despite low training losses. In our experiments, the optimal balance emerges at $e = -0.5$, which achieves the lowest test error for two reasons. First, it maintains reasonable approximation quality for large modes (better than $e = -1$). Second, it meaningfully improves intermediate and small modes (better than $e \geq 0$). For $e > 0$, the optimizer neglects small modes, with their losses exceeding base levels, i.e., higher loss than zero coefficients. Only the first 10, 8, and 5 modes improve for $e = 0.0, 0.5$, and 1.0 respectively, showing how increased emphasis on large modes comes at the expense of all others.

This analysis reveals a fundamental insight: The standard loss function ($e = 0$) is poorly calibrated for the multi-scale nature of the mode decomposition. The steep singular value decay creates an optimization landscape where gradients are dominated by a small subset of modes, leaving most of the representation capacity unused.

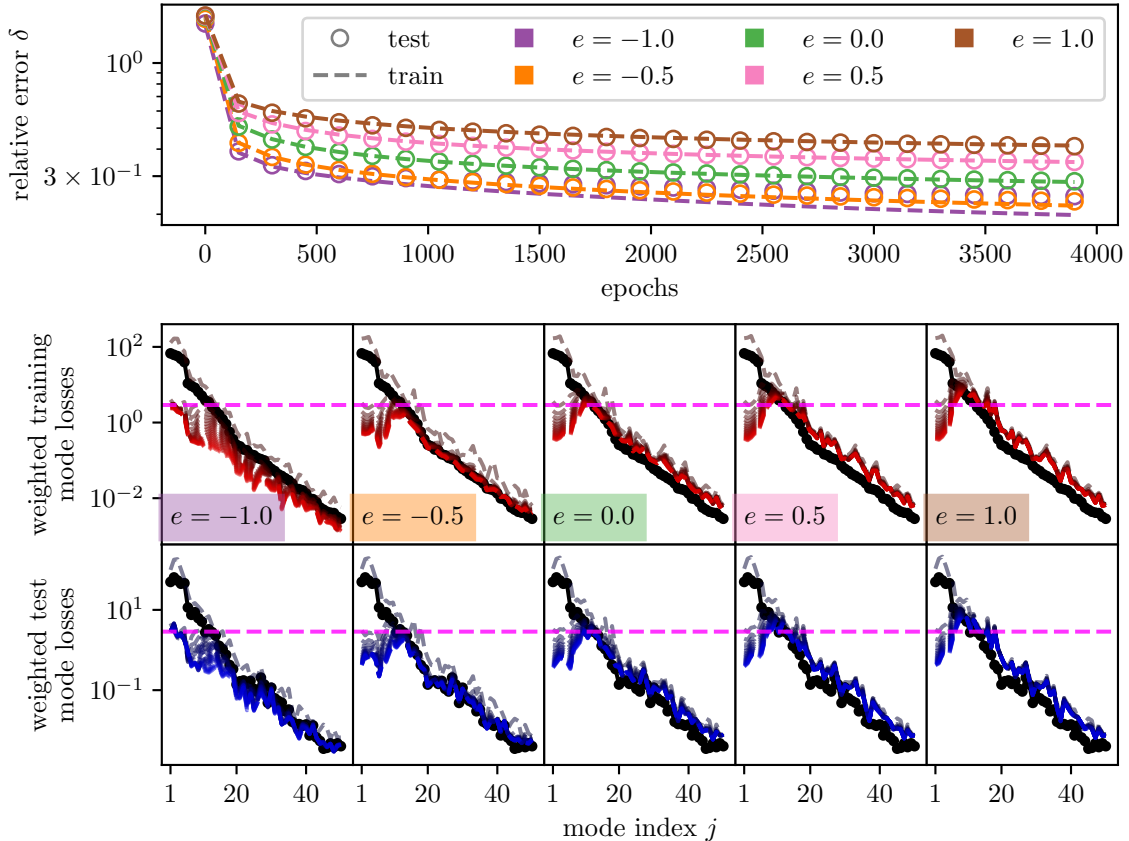


Figure 4: **Model performance across different exponents e and training epochs for DeepONets trained using GD.** **Top panel:** Relative error $\delta = \|A - \hat{A}\|_F / \|A\|_F$ for both training (dashed lines) and test (circles) data across different exponents ($e = -1.0, -0.5, 0.0, 0.5, 1.0$) over 4000 epochs. **Center and bottom row:** Weighted training (center row) and test (bottom row) mode losses at different training stages, colored from gray (initial) to red/blue (final). Each column corresponds to a different exponent e . The third column shows the DeepONet trained using the standard loss ($e = 0$). The plots in the center and bottom row contain the respective base losses in black, and a pink dashed horizontal line marking the maximum mode loss in the last training epoch of $e = 0$, facilitating comparison between different exponents e .

6.3.3 Adam Optimizer

The Adam optimizer provides an alternative to the gradient imbalance problem through its adaptive learning rate mechanism. Figure 5 shows that Adam achieves significantly lower total losses than GD with standard weighting, and its mode loss distribution is more similar to GD with $e \approx -0.5$ or -1.0 .

Unlike GD with $e = 0$, Adam reduces all training mode losses below their base values, even for small modes, though at different rates. The optimizer achieves significant loss reduction on approximately 30 modes for both training and test data, whereas GD effectively improves only the first ten. This suggests that Adam’s per-parameter learning rate adaptation compensates for the singular value imbalance, effectively implementing an implicit re-weighting scheme.

The mode loss distribution under Adam can be characterized as follows: Large modes ($i \lesssim 10$) are well-approximated with low weighted losses. Note that Adam approximates the large modes far better than GD (cf. fig. 3). Small modes ($i \gtrsim 30$) contribute negligibly due to tiny singular values. The intermediate modes’ losses are significantly improved compared to base losses but still contribute significantly to the total error due to non-negligible singular values. Furthermore, note that large modes have a significantly higher contribution to the test loss compared to the training loss. When explicitly re-weighting Adam ($e \neq 0$), we observe that $e = -1.0$ yields approximately homogeneous unweighted mode losses $L_{i,\text{tr}} \approx \text{constant}$ for the training data; this can be inferred from the weighted mode losses in section H.1, since the weighting factor σ_i^2 is known. However, similar to GD, aggressive emphasis on

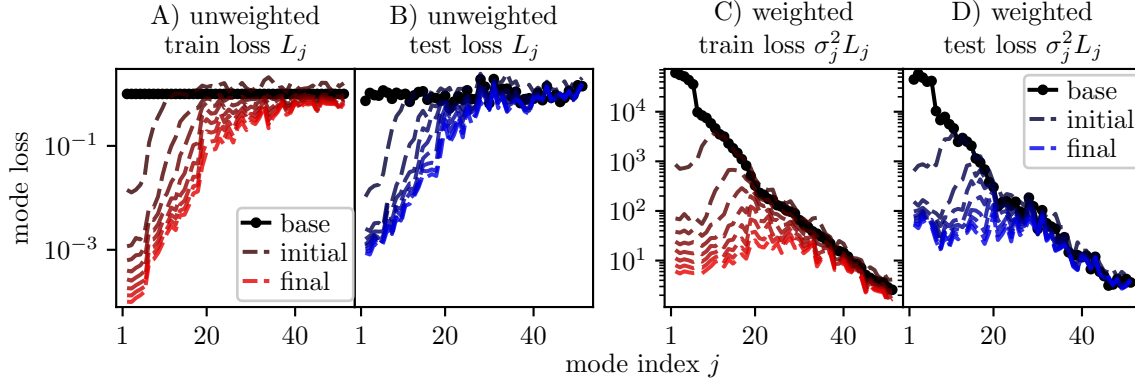


Figure 5: **Weighted mode losses for DeepONet trained with Adam.** Unweighted (A,B) and weighted (C,D) training (A,C) and test (B,D) mode losses at different training stages, colored from gray (initial) to red/blue (final) shown as dashed lines. The respective base losses are shown as black dot-solid lines.

small modes ($e < 0$) leads to overfitting. For Adam, we observe optimal test performance at $e = 0$. This indicates that Adam’s implicit re-weighting already strikes a good balance for generalization.

Remark 5. The superior performance of adaptive gradient methods extends beyond Adam; for instance, AdaGrad shows similar improvements over standard GD (see section H.2). This consistent pattern suggests that addressing the gradient imbalance through adaptive learning rates is crucial for operator learning tasks where the loss function admits a multi-scale decomposition.

6.4 Mechanisms Influencing the Mode Loss Distribution

Having established how different optimizers affect the mode loss distribution, we now investigate the underlying mechanisms driving these patterns. We examine three complementary perspectives: spectral bias in neural networks, (some) architectural design choices, and parameter-space coupling between modes.

6.4.1 Spectral Bias

Spectral bias [46, 68] is the tendency of neural networks to learn low-frequency components faster and more accurately than high-frequency ones. We investigate whether this affects the branch network’s mode loss distribution.

Since section 5 shows trunk error is negligible for large N , we focus on the branch network. The modification in section 6.1 provides well-defined target functions for analysis: the j -th branch neuron predicts V_{kj} for input p_k , defining the *right singular function* $\rho_j : p_k \mapsto V_{kj}$. If spectral bias affects the branch, mode losses L_j should correlate with ρ_j frequency: high-frequency ρ_j should yield higher losses.

We define the function frequency of $g : \mathbb{R}^d \rightarrow \mathbb{R}$ using the Fourier transform $\mathcal{F}(g)(\xi) = \int_{\mathbb{R}^d} g(x) \exp(-2\pi i \xi^T x) dx$.

The mean frequency [69] is $f(g) = \frac{\int_{\mathbb{R}^d} |\mathcal{F}(g)(\xi)|^2 \|\xi\|_2 d\xi}{\int_{\mathbb{R}^d} |\mathcal{F}(g)(\xi)|^2 d\xi}$. We first investigate spectral bias in the branch network on a synthetic dataset with curated spectral properties. As described in more detail in section I.1, the synthetic data is created such that the mean frequency of ρ_j is

$$f(\rho_j) \approx \begin{cases} F_0 \exp(\alpha(j-1)) & \text{if } \alpha > 0, \\ F_0 \exp(\alpha(j-1-N)) & \text{else.} \end{cases}$$

Thus, F_0 denotes the minimum frequency and α denotes the rate of increase (or decrease) of the frequencies.

We set the singular values to $\sigma_j = \exp(\beta j)$. Since $\beta = 0$ makes the ordering of right singular vectors non-unique, we require $\beta \neq 0$. Firstly, we consider $|\beta|$ small to isolate spectral bias effects from singular value weighting. For instance, $\beta = -0.01$ in fig. 6 (top) yields $\sigma_1^2/\sigma_5^2 \approx 1.08$, so all modes are approximately equally relevant while remaining correctly ordered. We then compare two cases: (i) $\alpha = 0.2$ and (ii) $\alpha = -0.2$. The mode losses in both cases are very similar, and in both cases, the low-frequency modes have smaller mode losses. In fig. 6 (bottom), we consider the same frequencies $\alpha = \pm 0.2$, but $\beta = -0.5$, i.e., a strong prioritization of the first few modes ($\sigma_1^2 \approx 55\sigma_5^2$). Here, we see that despite the initially slower learning of the higher-frequency features, they are eventually learned due to their higher relevance. This illustrates the competing effects of loss weighting and spectral bias.

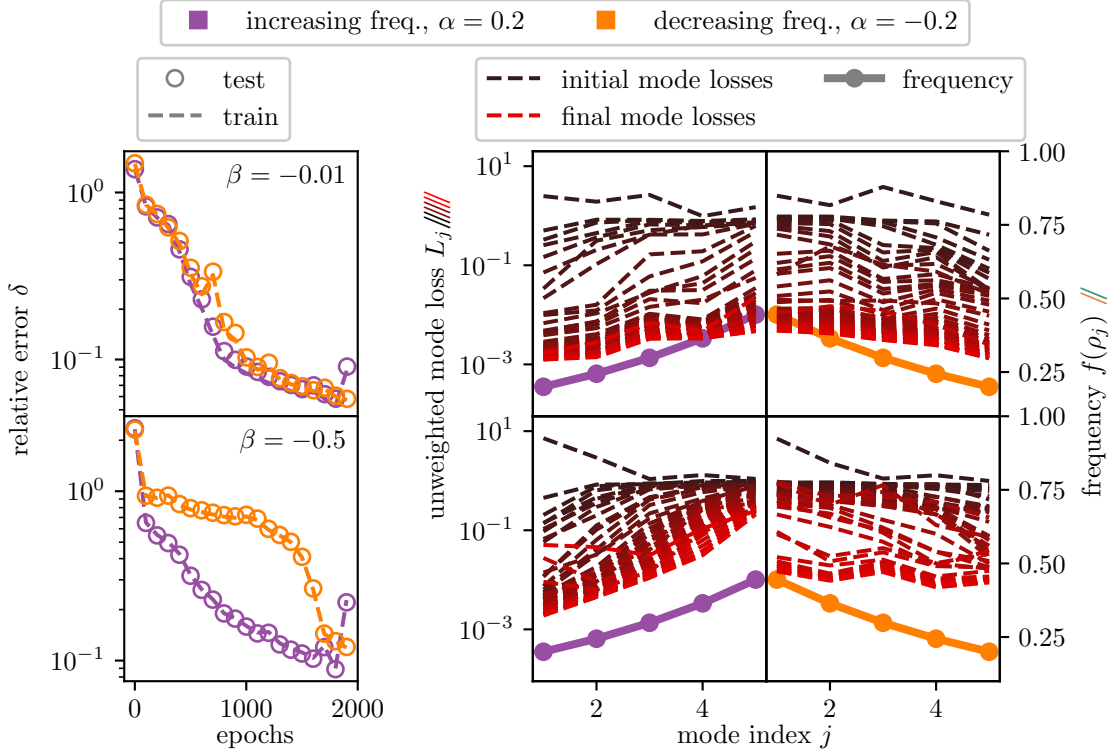


Figure 6: **Spectral bias in modified DeepONet for synthetic data.** **Left:** Relative error over epochs (training error as dashed line and test error as circles; nearly identical). **Center/right:** Unweighted mode losses (left scale) at different training stages (colored from black (initial) to red (final)) with frequencies of right singular functions (right scale). The center column shows the case of increasing frequencies ($\alpha = 0.2$), and the right column shows the case of decreasing frequencies ($\alpha = -0.2$); the corresponding relative errors are shown in purple and orange respectively in the left column. **Top/bottom:** The top row shows synthetic data with singular values $\sigma_j = \exp(-0.01j)$, while the bottom row has $\sigma_j = \exp(-0.5j)$.

We now return to the PDE datasets (advection-diffusion, KdV, and Burgers) and investigate the impact of spectral bias on the mode loss distribution. The (inverse) scaled singular values $1/\sigma_i^{0.2}$, the unweighted mode losses, and the frequencies $f(\rho_i)$ of the right singular functions ρ_i are shown in fig. 7 for the following considered example problems: advection-diffusion with $\tau = 0.5$, KdV with $\tau = 0.2$, KdV with $\tau = 0.6$, and Burgers with $\tau = 0.1$. To show the trend of the frequencies of ρ_i , we choose two methods to estimate the frequencies: the total variation (TV) norm and the Laplacian energy (LE). The TV norm estimates frequency by measuring how rapidly the function values change between neighboring samples, while the LE uses concepts from spectral graph theory to quantify oscillations on a graph constructed from the data. Both methods are k -nearest neighbor methods; we use $k = 3$ and $k = 50$ for the TV norm and LE, respectively. A detailed description of both methods can be found in section I.2. Note that each plot in fig. 7 contains two y -axis scales, left and right, both logarithmic.

For the KdV and Burgers equations (second–fourth columns in fig. 7), we observe a clear correlation between $f(\rho_i)$ and the mode losses L_i for both test and training data. Since both test and training mode losses are low for low frequencies and high for high frequencies, the branch network learns a generalizing approximation for low frequencies while underfitting high frequencies.

For the advection-diffusion equation (first column), the estimated frequencies $f(\rho_i)$ vary only weakly with i . Unlike the KdV and Burgers equations, no general trend is observable. However, we observe an approximately constant test mode loss $L_{i,te}$, indicating significant overfitting. Due to the different input dimensions M across the example problems, a reliable method to compare the frequencies of the ρ_i between problems is not available. Consequently, an explanation based on spectral bias for why the DeepONet overfits the advection-diffusion equation compared to other equations cannot be given. An alternative hypothesis, unrelated to spectral bias, is that the advection-diffusion problem’s low rank (exactly 20, matching the inner dimension N) removes the approximation pressure present in higher-rank problems like KdV, potentially allowing the network to memorize training data without learning general-

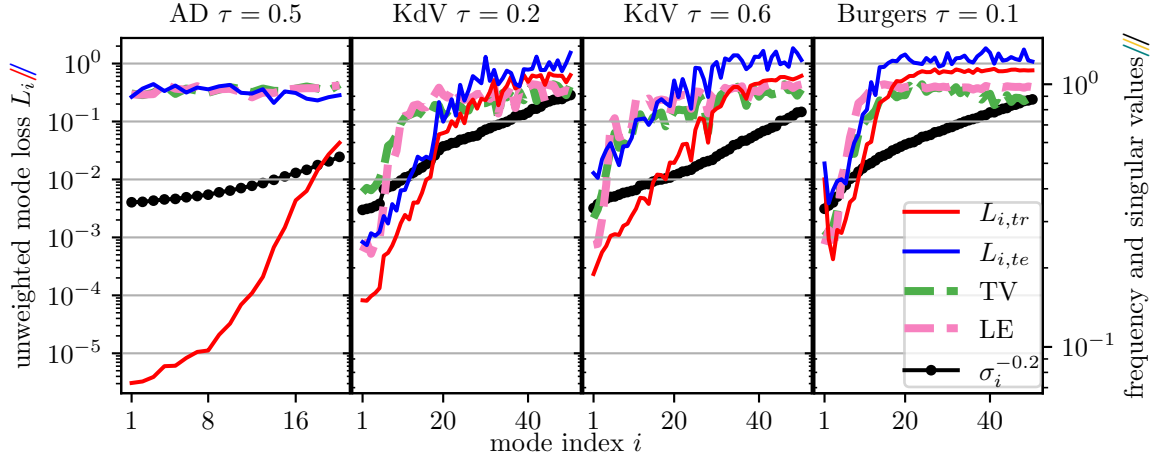


Figure 7: **Spectral bias in modified DeepONet for different PDEs.** Unweighted training (red) and test (blue) mode losses (left scale), the frequencies (right scale) of the right singular functions ρ_i estimated via the TV norm with $k = 3$ (green) and LE $k = 50$ (pink) and the scaled singular values $\sigma_i^{-0.2}$ (black, right scale) are shown. **Example problems (by column):** advection-diffusion (AD) equation with $\tau = 0.5$, KdV equation with $\tau = 0.2$, KdV equation with $\tau = 0.6$ and Burgers’ equation with $\tau = 0.1$.

izable structure, thus resulting in uniform overfitting across all modes. However, confirming this hypothesis requires further investigation in future work.

6.4.2 Architectural Coupling

Both the standard and the modified DeepONet, Section 6.1, use a single branch network with shared hidden layers outputting all mode coefficients simultaneously. However, together with the normal (or unstacked) DeepONet, Lu et al. also proposed the so-called stacked DeepONet [4]. Instead of one multi-layer perceptron with N output neurons, the branch network in the stacked DeepONet consists of N multi-layer perceptrons with one output neuron each, see fig. 8a. We thus say that the coefficients are *architecturally coupled* in the unstacked DeepONet.

To investigate the influence of architectural coupling, we compare the performance of stacked and unstacked DeepONets. Specifically, we use a stacked DeepONet whose branch networks each have depth $D = 5$ and hidden layer width $w_{sta} = 42$. We compare this to an unstacked DeepONet with the same number of trainable parameters. To achieve this, we choose $w_{unst} = 495$ and $D = 5$.

Figure 8b and 8c show the total loss over training and the mode losses of the stacked and unstacked DeepONets, respectively. The stacked DeepONet achieves a lower training error, while the unstacked DeepONet achieves a slightly lower test error, indicating overfitting in the stacked DeepONet. The mode losses show that the stacked DeepONet does not overfit uniformly across modes. For large modes, the stacked DeepONet achieves the smallest test and training errors. However, for small modes, the stacked DeepONet’s low training losses do not transfer to the test data. Even for intermediate modes, the unstacked network generalizes significantly better than the stacked DeepONet.

The first key observation from section 6.3 was that small modes seem to generalize poorly when fitted well on training data. The stacked DeepONet experiments corroborate this hypothesis. Furthermore, we observe that unstacking, or neuron-sharing, helps overall generalizability but not for all modes. In particular, it seems to negatively impact the training loss and generalizability of large modes while improving the generalizability of smaller modes.

Remark 6. This counterintuitive result connects to insights from MTL [52]. Recall that the shared hidden layers in the unstacked architecture force the network to learn representations that work across multiple modes. When different tasks (here, approximating different mode coefficients) share an underlying structure, this parameter sharing acts as an implicit regularizer, promoting sets of parameters that generalize well rather than overfitting to individual modes. This implies that even when practitioners require only specific modes (e.g., the coefficients for specific spatial frequencies), the unstacked architecture may still be preferable. The parameter sharing facilitates learning of generalizable features that improve approximation quality for target modes, even if other outputs are discarded. Note that this is a different connection to MTL than works such as [70, 16, 71] draw; they train a so-called foundation model on different PDEs, while we consider multiple tasks within one PDE.

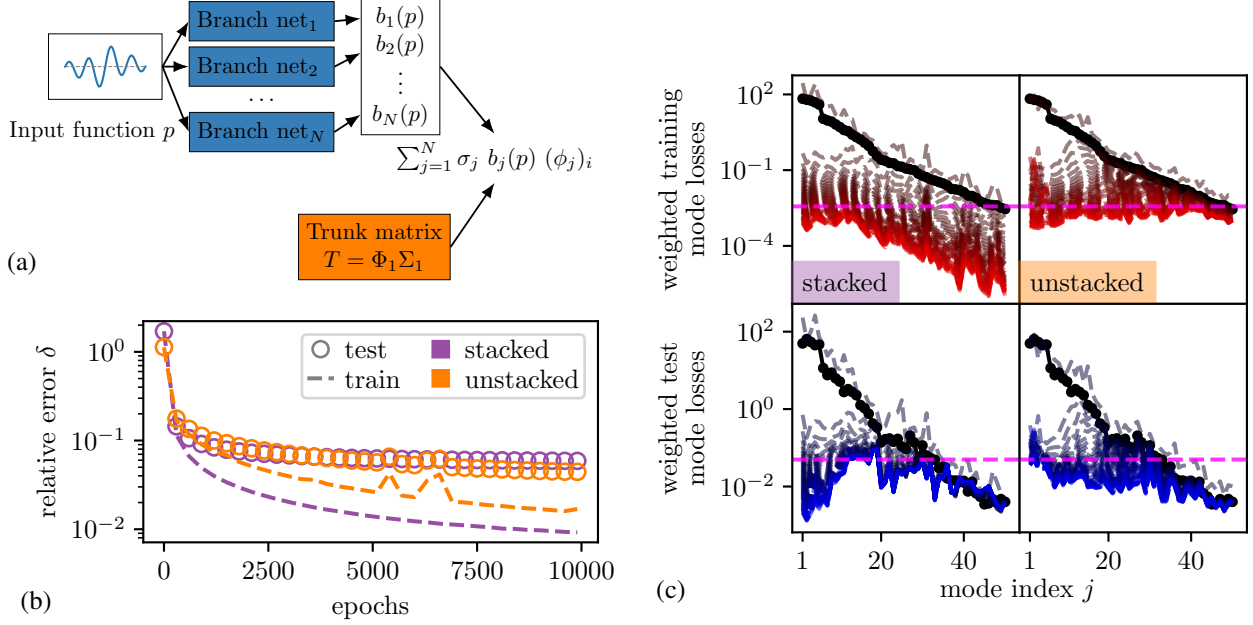


Figure 8: **Stacked and unstacked DeepONets.** (a) **Architecture of the stacked modified DeepONet.** Figure 1 (bottom left) shows the unstacked DeepONets for reference. Adapted and reproduced from [4]. (b) **Relative errors for stacked and unstacked DeepONets trained with Adam.** (c) **Weighted mode losses for stacked and unstacked DeepONets trained with Adam.** Weighted training (top row) and test (bottom row) mode losses at different training steps, colored from gray (initial) to red/blue (final). Columns correspond to different architectures and hidden layer widths (left: stacked with $w_{sta} = 42$, right: unstacked with $w_{unst} = 495$), as indicated by the labels. The center and bottom row plots also contain the respective base losses in black, and a pink dashed horizontal line marking the maximum mode loss of the fully-trained unstacked DeepONet.

6.4.3 Update-Based Coupling

In comparing stacked and unstacked DeepONets, we investigated how rearranging the branch network so that modes have separated parameters (while keeping the number of parameters constant) affects generalization. In this section, we consider unstacked DeepONets and investigate further how much of the loss stems from mode coupling. We are concerned with the modes' coupling in parameter space. Changing the value of the i -th branch output neuron does not change the contribution of any other mode to the DeepONet output because of the modes' orthogonality ($\phi_i^T \phi_j = 0$ for $i \neq j$). However, when training with gradient descent to reduce the loss for mode i , this parameter update changes all network parameters, since they are shared between modes. Thus, the mode i -specific parameter update can significantly alter the values of all branch output neurons, not just the i -th one, due to the neuron-sharing discussed in section 6.4.2.

We now give a formal definition of *mode coupling in parameter space* for DeepONets trained with GD. Unless stated otherwise, any loss function in this section is evaluated at the current parameters θ , and gradients are computed with respect to θ . For clarity, we write ∇L_i instead of $\nabla_{\theta} L_i(\theta)$, and $\nabla \mathcal{L}$ instead of $\nabla_{\theta} \mathcal{L}(\theta)$. Consider a GD parameter update

$$\delta\theta = -\alpha \nabla \mathcal{L}_{tr} = -\frac{\alpha}{nm_{tr}} \sum_{j=1}^N \sigma_j^2 \nabla L_{j,tr},$$

where we also drop the iteration index t . Choosing a sufficiently small learning rate α allows us to approximate the change in the training and test loss function using a first-order Taylor expansion. As we will see, the Taylor expansion allows us to partition the loss change into coupling and non-coupling parts. The first-order Taylor expansion of the total loss (train or test) change $\Delta \mathcal{L}$ is

$$\Delta \mathcal{L} \approx (\nabla \mathcal{L})^T \delta\theta = \frac{1}{nm_{tr}} \sum_{i=1}^N \sigma_i^2 (\nabla L_i)^T \delta\theta = -\frac{\alpha}{n^2 m_{tr}^2} \sum_{i=1}^N \sum_{j=1}^N \sigma_i^2 \sigma_j^2 (\nabla L_i)^T \nabla L_{j,tr} =: d + \Omega,$$

where

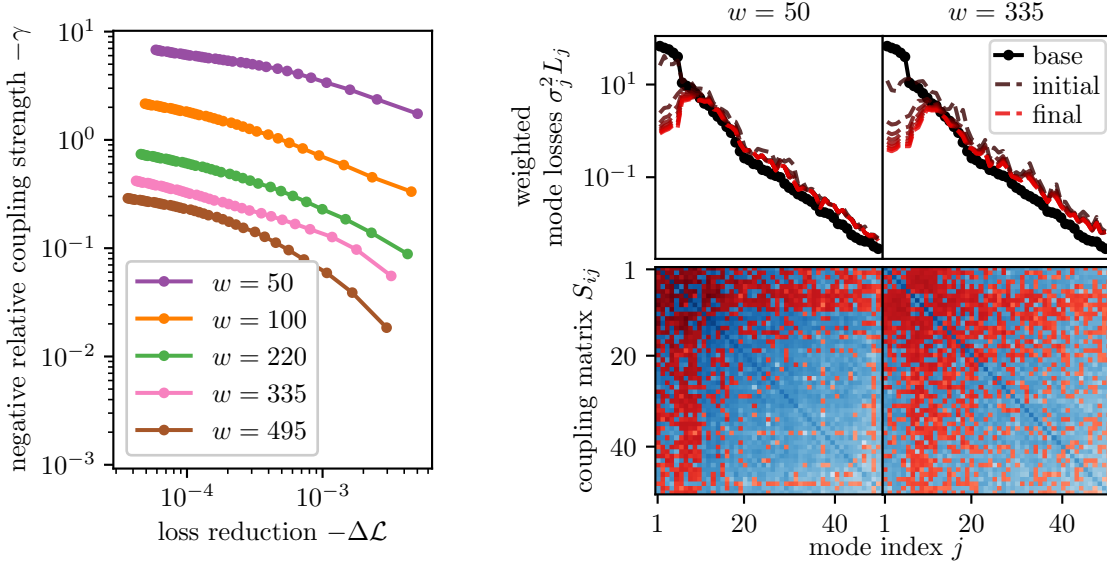
$$d =: -\frac{\alpha}{n^2 m_{tr}^2} \sum_{i=1}^N \sigma_i^4 (\nabla L_i)^T \nabla L_{i,tr} \quad \text{and} \quad \Omega =: -\frac{\alpha}{n^2 m_{tr}^2} \sum_{i=1}^N \sum_{j \neq i} \sigma_i^2 \sigma_j^2 (\nabla L_i)^T \nabla L_{j,tr}.$$

We call d the *diagonal term* and Ω is the *off-diagonal term*. Note that $d_{tr} \leq 0$, by definition. Then, we define the relative coupling strength as

$$\gamma := \frac{\Omega}{d + \Omega}.$$

Assume successful training, i.e., $d + \Omega < 0$, then detrimental coupling between the modes, i.e., $\Omega > 0$, is symbolized by $\gamma < 0$, while beneficial coupling $\Omega < 0$ is symbolized by $\gamma > 0$. Furthermore, training and test performance of DeepONets trained with GD have so far been observed to be very similar; these DeepONets are underfitting. We thus only explicitly focus on discussing the results for the training data.

We can now compute γ over the course of the training for different DeepONets. Figure 9a plots the (negative) relative coupling strength over the loss reduction for DeepONets of different hidden layer widths. For all hidden layer widths we find detrimental coupling, $\gamma < 0$. Furthermore, we find strong decoupling with increased width; i.e., the wider DeepONets exhibit significantly smaller negative coupling strengths. Note that these wider, decoupled DeepONets also achieve lower test and training losses.



(a) **Negative relative coupling strength $-\gamma$ plotted over loss reduction $-\Delta\mathcal{L}$ for DeepONets of different hidden-layer widths w .** The figure shows models with hidden layer widths 50 (purple), 100 (orange), 220 (green), 335 (pink) and 495 (brown).

(b) **Mode losses and coupling matrices.** **Top row:** Weighted mode losses at different training stages, colored from gray (initial) to red (final). Singular values shown in black. **Bottom row:** Entries of S_{tr} matrix after 4000 epochs. Red entries indicates a positive entry and blue indicates a negative entry (same colorscale for both matrices). **Left / right:** Hidden layer width $w = 50$ / $w = 335$.

Figure 9: Update-based coupling for DeepONets of different hidden-layer widths.

Furthermore, we can inspect the coupling directly by defining the coupling matrix $S \in \mathbb{R}^{N \times N}$ with entries

$$S_{ij} = -\frac{\alpha}{n^2 m_{tr}^2} \sigma_i^2 \sigma_j^2 (\nabla L_i)^T \nabla L_{j,tr}.$$

Thus, $d + \Omega = \sum_{i,j=1}^N S_{ij}$. Figure 9b shows the mode losses and the coupling matrices for DeepONets with $w = 50$ and $w = 335$. They both share a pattern: most entries in the first 10 rows and columns are positive (red). This means that the coupling between any two modes i, j is likely to be detrimental if $i \leq 10$. The pattern is less distinct in the wider DeepONet but still clearly visible. We furthermore note that only the first 10 modes' losses are significantly lower than their base losses; we thus refer to them (a bit euphemistically) as *well-approximated*. Thus, the coupling between a well-approximated mode and any other mode is likely to be detrimental. However, the coupling between two poorly approximated modes ($i, j > 10$) is likely to be beneficial; $S_{ij} < 0$ (blue).

7 Conclusion and Discussion

Trunk and Branch Error in DeepONets We decompose DeepONet error into trunk and branch components, adapting Lanthaler et al. [27]. Across PDE examples, the branch network (learning basis coefficients) dominates approximation error for large inner dimensions, while the trunk learns a sufficient basis. To the best of the authors’ knowledge, this is the first empirical, systematic investigation of the error distribution between basis and coefficient.

Modified DeepONet with Fixed SVD Basis To further investigate the branch error, we construct a modified DeepONet with a fixed SVD basis and briefly compare it to the standard DeepONet. For simplicity, we assume the standard SVD algorithm for a full data matrix, that is, the data must be sampled on the same spatial grid for every parameter configuration. This is computationally intensive and may not be feasible in higher-dimensional spatial domains, where the number of grid points grows exponentially with the spatial dimension (curse of dimensionality), but facilitates our analysis. The standard DeepONet is less restrictive regarding its training data. Furthermore, the modified DeepONet can only be evaluated on specific grid positions – however, if interpolation is used in the trunk, the modified DeepONet could be evaluated on all possible positions, similar to the standard DeepONet, though this is beyond the scope of the present work. We believe that our findings regarding the modified DeepONet are transferable to the standard DeepONet, since the standard DeepONet’s trunk network learns to approximate the SVD basis.

Mode Decomposition of the Branch Error Mode-specific analysis (enabled by the DeepONet modification) reveals poor generalization for modes with small singular values. Furthermore, distinct but characteristic mode loss distributions for DeepONets trained with GD and Adam can be observed. This highlights GD’s failure to capture more than the largest few modes. Three complementary effects shape this distribution: Spectral bias causes large errors for high-frequency modes, though its impact on generalization remains unclear. Architectural coupling (stacked vs. unstacked) produces different mode loss distributions and generalization, connecting operator learning to multi-task learning. Update-based coupling shows network width reduces mode interactions. These effects interact: right singular function frequency affects coefficient learnability, while parameter sharing in unstacked architectures further impacts approximation quality and training dynamics.

Practical Implications Network width is crucial for reducing mode coupling. MTL methods [72, 73] for gradient conflicts may address mode coupling in DeepONets. Adaptive optimizers (e.g., Adam) help learn beyond dominant modes, and unstacked architectures improve generalization through parameter sharing. Training data SVD can inform hyperparameter choices like inner dimension. The modified DeepONet and mode-decomposition analysis provide tools for understanding and improving operator learning.

Limitations and Future Work While our analysis focuses on time evolution operators, the error decomposition framework is not inherently restricted to this setting and may extend to other operator types, such as steady-state solution operators, integral operators, and parameter-to-solution maps. Open questions remain, in part due to our focus on relatively smooth PDE solutions. It is not clear how our analysis would change when the trunk error becomes more pronounced, for instance, for hyperbolic equations with discontinuous initial conditions or shock formations. Moreover, we have only considered low-dimensional spatial problems. Future work should address these scenarios and extend the analysis to different training and testing grids through an interpolator. Additionally, extending this analysis to more advanced DeepONet variants and architectures, such as those with Fourier features or Kolmogorov-Arnold networks, is an important direction for future work. Lastly, to clarify the impact of spectral bias, future work should include more example problems with varied spectral properties and improved frequency estimation methods.

8 CRediT authorship contribution statement

Alexander Heinlein: Conceptualization, Methodology, Investigation, Writing - review and editing, Supervision
Johannes Taraz: Conceptualization, Methodology, Software, Validation, Investigation, Writing - original draft, Writing - review and editing, Visualization

9 Declaration of competing interest

The authors declare that they have no known competing financial interests or personal relationships that could have appeared to influence the work reported in this paper.

10 Code availability statement

The implementation is available at <https://github.com/jotaraz/ModeDecomposition-DeepONets>.

11 Acknowledgments

We thank Henk Schuttelaars for conceptual discussions during the early stages of this work and for feedback on related drafts.

12 Declaration of generative AI in the manuscript preparation process

During the preparation of this work the authors used Claude [74] for proof-reading and language revision. After using this tool, the authors reviewed and edited the content as needed and take full responsibility for the content of the published article.

References

- [1] T. O. de Jong, K. Shukla, M. Lazar, Deep Operator Neural Network Model Predictive Control, preprint, arXiv:2505.18008 (2025). doi:10.48550/arXiv.2505.18008.
- [2] D. R. Sarkar, J. Drgoňa, S. Goswami, Learning to Control PDEs with Differentiable Predictive Control and Time-Integrated Neural Operators, preprint, arXiv:2511.08992 (2025). doi:10.48550/arXiv.2511.08992.
- [3] K. Bhattacharya, B. Hosseini, N. B. Kovachki, A. M. Stuart, Model Reduction And Neural Networks For Parametric PDEs, SMAI J. Comput. Math. 7 (2021) 121–157. doi:10.5802/smai-jcm.74.
- [4] L. Lu, P. Jin, G. Pang, Z. Zhang, G. E. Karniadakis, Learning Nonlinear Operators via DeepONet Based on the Universal Approximation Theorem of Operators, Nat. Mach. Intell. 3 (3) (2021) 218–229. doi:10.1038/s42256-021-00302-5.
- [5] N. Kovachki, Z. Li, B. Liu, K. Azizzadenesheli, K. Bhattacharya, A. Stuart, A. Anandkumar, Neural Operator: Learning Maps Between Function Spaces with Applications to PDEs, J. Mach. Learn. Res. 24 (89) (2023) 1–97. URL <https://www.jmlr.org/papers/v24/21-1524.html>
- [6] B. Raonić, R. Molinaro, T. De Ryck, T. Rohner, F. Bartolucci, R. Alaifari, S. Mishra, E. de Bézenac, Convolutional Neural Operators for Robust and Accurate Learning of PDEs, in: Adv. Neural Inf. Process. Syst., Vol. 36, 2023, pp. 77187–77200.
- [7] P. Benner, M. Ohlberger, A. Patera, G. Rozza, K. Urban, Model Reduction of Parametrized Systems, Springer Cham, 2017. doi:10.1007/978-3-319-58786-8.
- [8] S. Chaturantabut, D. C. Sorensen, Discrete Empirical Interpolation for Nonlinear Model Reduction, in: Proceedings of the 48th IEEE Conference on Decision and Control (CDC), 2009, pp. 4316–4321. doi:10.1109/CDC.2009.5400045.
- [9] N. Baker, F. Alexander, T. Bremer, A. Hagberg, Y. Kevrekidis, H. Najm, M. Parashar, A. Patra, J. Sethian, S. Wild, K. Willcox, S. Lee, Workshop Report on Basic Research Needs for Scientific Machine Learning: Core Technologies for Artificial Intelligence (2019). URL <https://www.osti.gov/servlets/purl/1478744>
- [10] T. Chen, H. Chen, Universal Approximation to Nonlinear Operators by Neural Networks with Arbitrary Activation Functions and Its Application to Dynamical Systems, IEEE Trans. Neural Netw. 6 (4) (1995) 911–917. doi:10.1109/72.392253.
- [11] S. Liu, Y. Yu, T. Zhang, H. Liu, X. Liu, D. Meng, Architectures, Variants, and Performance of Neural Operators: A Comparative Review, Neurocomputing 648 (2025) 130518. doi:10.1016/j.neucom.2025.130518.
- [12] D. W. Abueidda, P. Pantidis, M. E. Mobasher, DeepOKAN: Deep Operator Network Based on Kolmogorov Arnold Networks for Mechanics Problems, preprint, arXiv:2405.19143 (2024). doi:10.48550/arXiv.2405.19143.
- [13] S. Wang, H. Wang, P. Perdikaris, Improved Architectures and Training Algorithms for Deep Operator Networks, J. Sci. Comput. 92 (2022) 35. doi:10.1007/s10915-022-01881-0.
- [14] S. Lee, Y. Shin, On the Training and Generalization of Deep Operator Networks, SIAM J. Sci. Comput. 46 (4) (2024) C273–C296. doi:10.1137/23M1598751.
- [15] A. A. Howard, M. Perego, G. E. Karniadakis, P. Stinis, Multifidelity Deep Operator Networks for Data-Driven and Physics-Informed Problems, J. Comput. Phys. 493 (2023) 112462. doi:10.1016/j.jcp.2023.112462.

- [16] V. Kumar, S. Goswami, K. Kontolati, M. D. Shields, G. E. Karniadakis, Synergistic Learning with Multi-Task DeepONet for Efficient PDE Problem Solving, *Neural Netw.* 184 (2025) 107113. doi:10.1016/j.neunet.2024.107113.
- [17] L. Lu, R. Pestourie, S. G. Johnson, G. Romano, Multifidelity Deep Neural Operators for Efficient Learning of Partial Differential Equations with Application to Fast Inverse Design of Nanoscale Heat Transport, preprint, arXiv:2204.06684 (2022). doi:10.48550/arXiv.2204.06684.
- [18] N. Boullé, C. J. Earls, A. Townsend, Data-Driven Discovery of Green's Functions with Human-Understandable Deep Learning, *Sci. Rep.* 12 (1) (2022). doi:10.1038/s41598-022-08745-5.
- [19] C. R. Gin, D. E. Shea, S. L. Brunton, J. N. Kutz, DeepGreen: Deep Learning of Green's Functions for Nonlinear Boundary Value Problems, *Sci. Rep.* 11 (2021). doi:10.1038/s41598-021-00773-x.
- [20] Q. Sun, S. Li, B. Zheng, L. Ju, X. Xu, Learning Singularity-Encoded Green's Functions with Application to Iterative Methods, preprint, arXiv:2509.11580 (2025). doi:10.48550/arXiv.2509.11580.
- [21] H. Melchers, J. Prins, M. Abdelmalik, Neural Green's Operators for Parametric Partial Differential Equations, preprint, arXiv:2406.01857 (2025). doi:10.48550/arXiv.2406.01857.
- [22] Z. Li, N. Kovachki, K. Aizzadenesheli, B. Liu, K. Bhattacharya, A. Stuart, A. Anandkumar, Fourier Neural Operator for Parametric Partial Differential Equations, in: *International Conference on Learning Representations (ICLR)*, 2021.
URL <https://openreview.net/forum?id=c8P9NQVtmn0>
- [23] B. Bahmani, S. Goswami, I. G. Kevrekidis, M. D. Shields, A Resolution Independent Neural Operator, preprint, arXiv:2407.13010 (2024). doi:10.48550/arXiv.2407.13010.
- [24] F. Bartolucci, E. de Bézenac, B. Raonić, R. Molinaro, S. Mishra, R. Alaifari, Representation Equivalent Neural Operators: A Framework for Alias-Free Operator Learning, in: *Adv. Neural Inf. Process. Syst.*, Vol. 36, 2023, pp. 69661–69672.
- [25] Q. Cao, S. Goswami, G. E. Karniadakis, Laplace Neural Operator for Solving Differential Equations, *Nat. Mach. Intell.* 6 (6) (2024) 631–640. doi:10.1038/s42256-024-00844-4.
- [26] N. Boullé, A. Townsend, Chapter 3 - A Mathematical Guide to Operator Learning, in: *Handbook of Numerical Analysis, Vol. 25 of Numerical Analysis Meets Machine Learning*, Elsevier, 2024, pp. 83–125. doi:10.1016/bs.hna.2024.05.003.
- [27] S. Lanthaler, S. Mishra, G. E. Karniadakis, Error Estimates for DeepONets: A Deep Learning Framework in Infinite Dimensions, *Trans. Math. Appl.* 6 (1) (2022) tnac001. doi:10.1093/imatrm/tnac001.
- [28] C. Schwab, A. Stein, J. Zech, Deep Operator Network Approximation Rates for Lipschitz Operators, preprint, arXiv:2307.09835 (2023). doi:10.48550/arXiv.2307.09835.
- [29] M. W. M. G. Dissanayake, N. Phan-Thien, Neural-Network-Based Approximations for Solving Partial Differential Equations, *Commun. Numer. Methods Eng.* 10 (3) (1994) 195–201. doi:10.1002/cnm.1640100303.
- [30] I. Lagaris, A. Likas, D. Fotiadis, Artificial Neural Networks for Solving Ordinary and Partial Differential Equations, *IEEE Trans. Neural Netw.* 9 (5) (1998) 987–1000. doi:10.1109/72.712178.
- [31] M. Raissi, P. Perdikaris, G. E. Karniadakis, Physics-Informed Neural Networks: A Deep Learning Framework for Solving Forward and Inverse Problems Involving Nonlinear Partial Differential Equations, *J. Comput. Phys.* 378 (2019) 686–707. doi:10.1016/j.jcp.2018.10.045.
- [32] S. Goswami, A. Bora, Y. Yu, G. E. Karniadakis, Physics-Informed Deep Neural Operator Networks, in: *Machine Learning in Modeling and Simulation, Computational Methods in Engineering & the Sciences*, Springer, Cham, 2023. doi:10.1007/978-3-031-36644-4_6.
- [33] S. Wang, H. Wang, P. Perdikaris, Learning the Solution Operator of Parametric Partial Differential Equations with Physics-Informed DeepONets, *Sci. Adv.* 7 (40) (2021) eabi8605. doi:10.1126/sciadv.abi8605.
- [34] R. Bischof, M. Piovrač, M. A. Kraus, S. Mishra, B. Bickel, HyPINO: Multi-Physics Neural Operators via HyperPINNs and the Method of Manufactured Solutions, preprint, arXiv:2509.05117 (2025). doi:10.48550/arXiv.2509.05117.
- [35] V. Grimm, A. Heinlein, A. Klawonn, Learning the Solution Operator of Two-Dimensional Incompressible Navier-Stokes Equations Using Physics-Aware Convolutional Neural Networks, *J. Comput. Phys.* 535 (2025) 114027. doi:10.1016/j.jcp.2025.114027.
- [36] L. Mandl, S. Goswami, L. Lambers, T. Ricken, Separable Physics-Informed DeepONet: Breaking the Curse of Dimensionality in Physics-Informed Machine Learning, *Comput. Methods Appl. Mech. Eng.* 434 (2025) 117586. doi:10.1016/j.cma.2024.117586.
- [37] D. Nayak, S. Goswami, TI-DeepONet: Learnable Time Integration for Stable Long-Term Extrapolation, preprint, arXiv:2505.17341 (2025). doi:10.48550/arXiv.2505.17341.

- [38] S. Wang, P. Perdikaris, Long-Time Integration of Parametric Evolution Equations with Physics-Informed DeepONets, preprint, arXiv:2106.05384 (2021). doi:10.48550/arXiv.2106.05384.
- [39] L. Lu, X. Meng, S. Cai, Z. Mao, S. Goswami, Z. Zhang, G. E. Karniadakis, A Comprehensive and Fair Comparison of Two Neural Operators (with Practical Extensions) Based on FAIR Data, *Comput. Methods Appl. Mech. Eng.* 393 (2022) 114778. doi:10.1016/j.cma.2022.114778.
- [40] S. Venturi, T. Casey, SVD Perspectives for Augmenting DeepONet Flexibility and Interpretability, *Comput. Methods Appl. Mech. Eng.* 403 (2023) 115718. doi:10.1016/j.cma.2022.115718.
- [41] V. S. Fanaskov, I. V. Oseledets, Spectral Neural Operators, *Dokl. Math.* 108 (2023) S226–S232. doi:10.1134/S1064562423701107.
- [42] S. Lanthaler, Operator Learning with PCA-Net: Upper and Lower Complexity Bounds, preprint, arXiv:2303.16317 (2023). doi:10.48550/arXiv.2303.16317.
- [43] H. Eivazi, S. Wittek, A. Rausch, Nonlinear Model Reduction for Operator Learning, preprint, arXiv:2403.18735 (2024). doi:10.48550/arXiv.2403.18735.
- [44] N. Demo, M. Tezzele, G. Rozza, A DeepONet Multi-Fidelity Approach for Residual Learning in Reduced Order Modeling, *Adv. Model. Simul. Eng. Sci.* 10 (2023). doi:10.1186/s40323-023-00249-9.
- [45] E. Williams, A. Howard, B. Meuris, P. Stinis, What Do Physics-Informed DeepONets Learn? Understanding and Improving Training for Scientific Computing Applications, preprint, arXiv:2411.18459 (2024). doi:10.48550/arXiv.2411.18459.
- [46] N. Rahaman, A. Baratin, D. Arpit, F. Draxler, M. Lin, F. Hamprecht, Y. Bengio, A. Courville, On the Spectral Bias of Neural Networks, in: *Proc. Mach. Learn. Res.*, Vol. 97, 2019, pp. 5301–5310. URL <https://proceedings.mlr.press/v97/rahaman19a.html>
- [47] S. Khodakarami, V. Oommen, A. Bora, G. E. Karniadakis, Mitigating Spectral Bias in Neural Operators via High-Frequency Scaling for Physical Systems, preprint, arXiv:2503.13695 (2025). doi:10.48550/arXiv.2503.13695.
- [48] Q. Kong, C. Zou, Y. Choi, E. M. Matzel, K. Azizzadenesheli, Z. E. Ross, A. J. Rodgers, R. W. Clayton, Reducing Frequency Bias of Fourier Neural Operators in 3D Seismic Wavefield Simulations Through Multi-Stage Training, preprint, arXiv:2503.02023 (2025). doi:10.48550/arXiv.2503.02023.
- [49] B. Wang, L. Liu, W. Cai, Multi-Scale DeepOnet (Mscale-DeepOnet) for Mitigating Spectral Bias in Learning High Frequency Operators of Oscillatory Functions, preprint, arXiv:2504.10932 (2025). doi:10.48550/arXiv.2504.10932.
- [50] E. Zhang, A. Kahana, A. Kopaničáková, E. Turkel, R. Ranade, J. Pathak, G. E. Karniadakis, Blending Neural Operators and Relaxation Methods in PDE Numerical Solvers, preprint, arXiv:2208.13273 (2024). doi:10.48550/arXiv.2208.13273.
- [51] A. Sojitra, M. Dhingra, O. San, FEDONet: Fourier-Embedded DeepONet for Spectrally Accurate Operator Learning, preprint, arXiv:2509.12344 (2025). doi:10.48550/arXiv.2509.12344.
- [52] S. Ruder, An Overview of Multi-Task Learning in Deep Neural Networks, preprint, arXiv:1706.05098 (2017). doi:10.48550/arXiv.1706.05098.
- [53] J. Choi, C.-O. Lee, M. Moon, Hybrid Least Squares/Gradient Descent Methods for DeepONets, preprint, arXiv:2508.15394 (2025). doi:10.48550/arXiv.2508.15394.
- [54] G. Cybenko, Approximation by Superpositions of a Sigmoidal Function, *Math. Control Signals Syst.* 2 (4) (1989) 303–314. doi:10.1007/BF02551274.
- [55] A. Pinkus, Approximation Theory of the MLP Model in Neural Networks, *Acta Numer.* 8 (1999) 143–195. doi:10.1017/S0962492900002919.
- [56] Y. LeCun, Y. Bengio, G. Hinton, Deep Learning, *Nature* 521 (2015) 436–444. doi:10.1038/nature14539.
- [57] D. Hendrycks, K. Gimpel, Gaussian Error Linear Units (GELUs), preprint, arXiv:1606.08415 (2023). doi:10.48550/arXiv.1606.08415.
- [58] Y. LeCun, L. Bottou, G. B. Orr, K.-R. Müller, *Neural Networks: Tricks of the Trade*, Springer, Berlin Heidelberg, 1998. doi:10.1007/3-540-49430-8_2.
- [59] S. K. Kumar, On Weight Initialization in Deep Neural Networks, preprint, arXiv:1704.08863 (2017). doi:10.48550/arXiv.1704.08863.
- [60] D. P. Kingma, J. Ba, Adam: A Method for Stochastic Optimization, in: *International Conference on Learning Representations (ICLR)*, 2015. URL <https://arxiv.org/abs/1412.6980>
- [61] D. Rumelhart, G. Hinton, R. Williams, Learning internal representations by error propagation, in: A. Collins, E. E. Smith (Eds.), *Readings in Cognitive Science*, Morgan Kaufmann, 1988, pp. 399–421. doi:<https://doi.org/>

- org/10.1016/B978-1-4832-1446-7.50035-2.
 URL <https://www.sciencedirect.com/science/article/pii/B9781483214467500352>
- [62] J. Duchi, E. Hazan, Y. Singer, Adaptive Subgradient Methods for Online Learning and Stochastic Optimization, *J. Mach. Learn. Res.* 12 (61) (2011) 2121–2159.
 URL <http://jmlr.org/papers/v12/duchi11a.html>
- [63] G. Hinton, Lecture 6e RMSprop: Divide the Gradient by a Running Average of Its Recent Magnitude, accessed 21.07.2025 (2012).
 URL https://www.cs.toronto.edu/~tijmen/csc321/slides/lecture_slides_lec6.pdf
- [64] G. H. Golub, C. F. V. Loan, *Matrix Computations*, Johns Hopkins University Press, 2013.
- [65] C. Eckart, G. Young, The Approximation of One Matrix by Another of Lower Rank, *Psychometrika* 1 (3) (1936) 211–218. doi:10.1007/BF02288367.
- [66] R. Tachet, M. Pezeshki, S. Shabanian, A. Courville, Y. Bengio, On the Learning Dynamics of Deep Neural Networks, preprint, arXiv:1809.06848 (2020). doi:10.48550/arXiv.1809.06848.
- [67] M. Pezeshki, S.-O. Kaba, Y. Bengio, A. Courville, D. Precup, G. Lajoie, Gradient Starvation: A Learning Proclivity in Neural Networks, preprint, arXiv:2011.09468 (2021). doi:10.48550/arXiv.2011.09468.
- [68] Z.-Q. J. Xu, Y. Zhang, Y. Xiao, Training Behavior of Deep Neural Network in Frequency Domain, preprint, arXiv:1807.01251 (2019). doi:10.48550/arXiv.1807.01251.
- [69] S. Mallat, *A Wavelet Tour of Signal Processing*, Academic Press, 2008, section 2.3.2.
- [70] M. Herde, B. Raonić, T. Rohner, R. Käppeli, R. Molinaro, E. de Bézenac, S. Mishra, Poseidon: Efficient Foundation Models for PDEs, preprint, arXiv:2405.19101 (2024). doi:10.48550/arXiv.2405.19101.
- [71] Z. Zhang, C. Moya, L. Lu, G. Lin, H. Schaeffer, DeepONet as a Multi-Operator Extrapolation Model: Distributed Pretraining with Physics-Informed Fine-Tuning, preprint, arXiv:2411.07239 (2024). doi:10.48550/arXiv.2411.07239.
- [72] T. Yu, S. Kumar, A. Gupta, S. Levine, K. Hausman, C. Finn, Gradient Surgery for Multi-Task Learning, in: *Adv. Neural Inf. Process. Syst.*, Vol. 33, 2020, pp. 5824–5836.
- [73] Z. Zhang, J. Shen, C. Cao, G. Dai, S. Zhou, Q. Zhang, S. Zhang, E. Shutova, Proactive Gradient Conflict Mitigation in Multi-Task Learning: A Sparse Training Perspective, preprint, arXiv:2411.18615 (2024). doi:10.48550/arXiv.2411.18615.
- [74] Anthropic, Claude, <https://www.anthropic.com> (2025).
- [75] K. Nakamura, B. Derbel, K.-J. Won, B.-W. Hong, Learning-Rate Annealing Methods for Deep Neural Networks, *Electronics* 10 (16) (2021) 2029. doi:10.3390/electronics10162029.
- [76] DeepMind, I. Babuschkin, K. Baumli, A. Bell, S. Bhupatiraju, J. Bruce, P. Buchlovsky, D. Budden, T. Cai, A. Clark, I. Danihelka, A. Dedieu, C. Fantacci, J. Godwin, C. Jones, R. Hemsley, T. Hennigan, M. Hessel, S. Hou, S. Kapturowski, T. Keck, I. Kemaev, M. King, M. Kunesch, L. Martens, H. Merzic, V. Mikulik, T. Norman, G. Papamakarios, J. Quan, R. Ring, F. Ruiz, A. Sanchez, L. Sartran, R. Schneider, E. Sezener, S. Spencer, S. Srinivasan, M. Stanojević, W. Stokowiec, L. Wang, G. Zhou, F. Viola, *The DeepMind JAX Ecosystem* (2020). URL <http://github.com/google-deepmind>
- [77] D. Zwicker, py-pde: A Python Package for Solving Partial Differential Equations, *J. Open Source Softw.* 5 (48) (2020) 2158. doi:10.21105/joss.02158.
- [78] M. Abramowitz, I. A. Stegun, *Handbook of Mathematical Functions with Formulas, Graphs, and Mathematical Tables*, Dover, New York, 1972, section 22.5.49 and 22.5.47.
- [79] C. Bishop, *Neural Networks for Pattern Recognition*, Oxford University Press, 1995.
- [80] T. Hastie, R. Tibshirani, J. Friedman, *The Elements of Statistical Learning*, Springer, 2009.
- [81] Y. Hu, R. Xian, Q. Wu, Q. Fan, L. Yin, H. Zhao, Revisiting Scalarization in Multi-Task Learning: A Theoretical Perspective, preprint, arXiv:2308.13985 (2023). doi:10.48550/arXiv.2308.13985.
- [82] L. Huang, J. Qin, Y. Zhou, F. Zhu, L. Liu, L. Shao, Normalization Techniques in Training DNNs: Methodology, Analysis and Application, *IEEE Trans. Pattern Anal. Mach. Intell.* 45 (8) (2023) 10173–10196. doi:10.1109/TPAMI.2023.3250241.
- [83] Z.-Q. J. Xu, Y. Zhang, T. Luo, Y. Xiao, Z. Ma, Frequency Principle: Fourier Analysis Sheds Light on Deep Neural Networks, *Commun. Comput. Phys.* 28 (5) (2020) 1746–1767. doi:10.4208/cicp. oa-2020-0085.
- [84] L. I. Rudin, S. Osher, E. Fatemi, Nonlinear Total Variation Based Noise Removal Algorithms, *Physica D* 60 (1) (1992) 259–268. doi:10.1016/0167-2789(92)90242-F.
- [85] P. Getreuer, Rudin-Osher-Fatemi Total Variation Denoising Using Split Bregman, *Image Process. Line* 2 (2012) 74–95. doi:10.5201/ipol.2012.g-tvd.

- [86] D. Spielman, Spectral and Algebraic Graph Theory, Yale Lecture Notes, 2025.
 URL <http://cs-www.cs.yale.edu/homes/spielman/sagt/>
- [87] T. Cover, P. Hart, Nearest Neighbor Pattern Classification, IEEE Trans. Inf. Theory 13 (1) (1967) 21–27. doi: 10.1109/TIT.1967.1053964.

A Appendix: Hyperparameters

The hyperparameters used in this work are similar to those employed in related works [4, 39, 45], balancing accuracy and cost. We use coarse hyperparameter search to maintain generality. Main findings (branch error dominance, mode loss distribution) remain qualitatively consistent across tested ranges: learning rates $[10^{-4}, 8 \times 10^{-3}]$, depths 3-10, widths 50-500, and different initializations.

The initial learning rate $\alpha_1 = 10^{-4}$, used throughout section 6.4.3, is chosen such that the first-order Taylor expansion of the loss change approximates the true loss change $\Delta\mathcal{L}$.

For every optimizer and every initial learning rate α_1 , the learning rate after t epochs, α_t , is given as

$$\alpha_t = 0.95^{\lfloor t/500 \rfloor} \cdot \alpha_1.$$

This is a common schedule in machine learning [75]. The Adam parameters are chosen following [76]: $\beta_1 = 0.9, \beta_2 = 0.999, \epsilon = 10^{-8}, \bar{\epsilon} = 0$.

Table 3 lists hyperparameters for all figures. *var1*: $\alpha_1 = 10^{-4}\sigma_1^{-2e}$ (see section 6.3.2). *var2, var3*: varying values for fig. 7 (AD: $N = 20, w = 332$; KdV: $N = 50, w = 335$; Burgers: $N = 20, w = 337$).

figure	example prob.	optimizer	α_1	depth	width	N	number of epochs
1	KdV $\tau = 0.2$	Adam	2×10^{-3}	5	100		5000
2	KdV $\tau = 0.2$	Adam	2×10^{-3}	5	100		5000
3	KdV $\tau = 0.2$	GD	10^{-4}	5	335	50	4000
4	KdV $\tau = 0.2$	GD	<i>var1</i>	5	335	50	4000
5	KdV $\tau = 0.2$	Adam	10^{-4}	5	335	50	4000
6	synth. data	Adam	2×10^{-3}	5	50	5	2000
7		Adam	10^{-4}	5	<i>var2</i>	<i>var3</i>	4000
8	KdV $\tau = 0.2$	Adam	10^{-4}	5		50	4000
9	KdV $\tau = 0.2$	GD	10^{-4}	5		50	4000
10	KdV $\tau = 0.2$	Adam	10^{-4}	5	335	50	4000
11	KdV $\tau = 0.2$		10^{-4}	5	335	50	4000

Table 3: **Hyperparameters of DeepONets and SVDONets used in each figure.** A cell is left empty, if there are multiple DeepONets shown in the figure and it is apparent which hyperparameter values correspond to which DeepONet. The term *varx* denotes a varying value for the different DeepONets which is not apparent from the figure. Each *varx* is explained in the text of this section.

B Appendix: Input Function Encoding

To eliminate encoding error [27], we restrict input functions to an L -dimensional subspace: $p(x) = \sum_{i=1}^L a_i \sin(i\pi x) \in \text{span}\{\sin(i\pi x)\}_{i=1}^L \subset \mathcal{C}([0, 1])$. Sampling on uniform mesh with M interior points $\bar{x}_j = \frac{j}{M+1}$ yields $\hat{p} = \Psi a \in \mathbb{R}^M$, where $\Psi_{ji} = \sin(i\pi \bar{x}_j)$ and $a \in \mathbb{R}^L$. For $M \geq L$, Ψ has full column rank, so coefficients recover exactly as $a = \Psi^+ \hat{p}$, yielding zero encoding error.

C Appendix: Data

For each example problem, the training and test data sets contain 900 and 100 input functions, respectively, both drawn from the same distribution. The input functions are of the form

$$p(x) = \sum_{i=1}^L a_i \sin(\omega_i x), \quad a_i \sim \mathcal{U}([-1, 1]),$$

with problem-specific parameters summarized in table 4.

problem	L	ω_i	τ	solver	n	M	$\text{rank}(A_{tr})$
AD	20	$2\pi i$	0.5, 1.0	FD + RK [77]	200	200	20
KdV	5	$2\pi i$	0.2, 0.6, 1.0	FD + RK [77]	400	400	400
Burgers	5	πi	0.1, 1.0	spectral (100 basis) + Euler	200	50	100

Table 4: Data generation parameters for the three example problems. Here, L is the number of input function modes, ω_i the corresponding frequencies, and FD + RK denotes the finite-difference method combined with a Runge–Kutta method.

The PDEs and boundary conditions for the KdV equation are given in section 3.5; the advection-diffusion (AD) and Burgers equations follow the same structure with the differential operators and boundary conditions specified below.

The AD equation is $\partial_t u + \frac{4}{2\pi} \partial_x u - \frac{0.01}{4\pi^2} \partial_x^2 u = 0$ with periodic boundary conditions on $(0, 1)$. Burgers’ equation is $\partial_t u + u \partial_x u - 0.01 \partial_x^2 u = 0$ with homogeneous Dirichlet boundary conditions on $(0, 1)$.

Range of test and training data matrices. For the AD equation, the solution operator is linear, so A_{tr} and A_{te} share the same 20-dimensional range and have rank 20. For the KdV equation; $\text{rank}(A_{tr}) = 400$ equals the spatial dimension n , the standard basis vectors of \mathbb{R}^{400} span $\text{ran}(A_{tr})$, implying $\text{ran}(A_{te}) \subset \text{ran}(A_{tr})$. For Burgers’ equation, the span of the discretized spectral basis functions equals the range of both data matrices. These containment properties are used in section G. Note that for the AD equation, the input functions must be sampled at $M \geq 2L$ interior meshpoints.

D Appendix: Bound on the Branch Error

As discussed in section 4.2.2 one can derive the following bound on the branch error.

$$\varepsilon_B \leq \|T\|_2^2 \|B^T - T^+ A\|_F^2 = \|T\|_2^2 \varepsilon_C =: \varepsilon_D$$

Table 5 shows the different error components, and the ratio between ε_B and ε_D for different N . Recall that, if ε_D were a tight bound on ε_B , the ratio would be ≈ 1 , i.e., $\log_{10}(\varepsilon_{D,te}/\varepsilon_{B,te}) \approx 0$. Note that the ratio increases as N increases, since the coefficients of more and more basis functions are poorly approximated.

N	$\log_{10} \varepsilon_{te}$	$\log_{10} \varepsilon_{T,te}$	$\log_{10} \varepsilon_{B,te}$	$\log_{10} \varepsilon_{D,te}$	$\log_{10}(\varepsilon_{D,te}/\varepsilon_{B,te})$
2	4.31	4.31	0.43	0.61	0.18
10	3.26	3.24	2.05	3.34	1.30
18	2.86	2.61	2.5	4.29	1.79
50	2.59	1.62	2.54	8.29	5.75
90	2.63	-0.31	2.63	13.48	10.86

Table 5: Total error, trunk error, branch error, upper bound on branch error $\varepsilon_D = \|T\|_2^2 \varepsilon_C$, and the ratio $\varepsilon_D/\varepsilon_B$.

E Appendix: Bases

We define the bases used in section 5. Except for the SVD basis vectors, all bases are families of functions $\{t_k\}_{k=1}^N \subset \mathcal{C}([0, 1])$. For the SVD basis, the k -th trunk network output is the k -th left singular vector of the training data matrix A , i.e., $t_k = \phi_k \in \mathbb{R}^n$. The learned basis functions are the trunk network outputs of a standard DeepONet. For the Legendre polynomials, we set $t_k(x) = P_{k-1}(2x - 1)$. Here P_k is the k -th Legendre polynomial, for instance, $P_0(x) = 1, P_1(x) = x, P_2(x) = (3x^2 - 1)/2 \dots$ [78]. For the Chebyshev polynomials, we set $t_k(x) = T_{k-1}(2x - 1)$. Here T_k is the k -th Chebyshev polynomial, for example, $T_0(x) = 1, T_1(x) = x, T_2(x) = 2x^2 - 1 \dots$ [78]. For the cosine harmonics, we set $t_k(x) = \cos((k - 1)\pi x)$.

F Appendix: Motivation for DeepONet Modification

We choose $T = \Phi_1 \Sigma_1$ for three reasons: (1) Φ_1 gives optimal rank- N approximation ($\varepsilon_T = \|\Sigma_2\|_F^2$); (2) using Σ_1 makes branch targets semi-orthogonal ($\|v_i\|_2^2 = 1$), a common normalization in machine learning [79, 80, 81, 82]; (3) simplifies analysis with straightforward unweighted mode loss L_i .

G Appendix: Deriving the Mode-Based Error Decomposition for Test Data

Since $\text{ran}(A_{te}) \subset \text{ran}(A_{tr})$, we have $A_{te} = \Phi \Sigma W^T$ with $W = (\Sigma^+ \Phi^T A_{te})^T$. Partitioning $W = [W_1 \ W_2]$ yields $A_{te} = \Phi_1 \Sigma_1 W_1^T + \Phi_2 \Sigma_2 W_2^T$, where $W_1 = (\Sigma_1^{-1} \Phi_1^T A_{te})^T$ contains optimal coefficients. The test error decomposes as

$$\varepsilon_{te} = \|\Sigma_1 B_{te}^T - \Sigma_1 W_1^T\|_F^2 + \|\Sigma_2 W_2^T\|_F^2 = \sum_{i=1}^N \sigma_i^2 \|b_{i,te} - w_i\|_2^2 + \|\Sigma_2 W_2^T\|_F^2.$$

Note: $A_{te} = \Phi \Sigma W^T$ is not an SVD, so Φ_1 lacks optimality for test data. Unlike training (V_1, V_2 semi-orthogonal), W_1, W_2 are not semi-orthogonal, so test trunk error could exceed training trunk error. However, this doesn't occur for our examples (see table 6).

problem		$\log_{10} \delta_{T,tr}$	$\log_{10} \delta_{T,te}$	$\log_{10} \delta_{T,tr}$	$\log_{10} \delta_{T,te}$	$\log_{10} \delta_{T,tr}$	$\log_{10} \delta_{T,te}$
		$N = 10$	$N = 10$	$N = 15$	$N = 15$	$N = 20$	$N = 20$
AD	$\tau = 0.5$	-0.41	-0.41	-0.78	-0.78	-12.6	-12.6
AD	$\tau = 1.0$	-0.69	-0.69	-1.32	-1.32	-13.1	-13.1
		$N = 30$	$N = 30$	$N = 50$	$N = 50$	$N = 70$	$N = 70$
KdV	$\tau = 0.2$	-1.48	-1.46	-2.19	-2.10	-2.94	-2.84
KdV	$\tau = 0.6$	-1.04	-1.03	-1.90	-1.88	-2.71	-2.59
KdV	$\tau = 1.0$	-1.00	-0.99	-1.91	-1.93	-2.70	-2.70
Burgers	$\tau = 0.1$	-1.36	-1.29	-1.90	-1.75	-2.42	-2.20
Burgers	$\tau = 1.0$	-3.56	-3.35	-5.53	-5.10	-7.54	-6.75

Table 6: Relative training and test trunk errors δ_T for all example problems (advection diffusion (AD), Korteweg-de Vries (KdV) and Burgers) and various N .

Furthermore, since the trunk error is determined by the choice of N , it can be omitted from the loss used in the neural network training. Thus, we use

$$\mathcal{L}_{tr} := \frac{1}{n_{tr} m_{tr}} \|\Sigma_1 B_{tr}^T - \Sigma_1 V_1^T\|_F^2 = \frac{1}{n_{tr} m_{tr}} \varepsilon_{B,tr}, \quad \mathcal{L}_{te} := \frac{1}{n_{te} m_{te}} \|\Sigma_1 B_{te}^T - \Sigma_1 W_1^T\|_F^2 = \frac{1}{n_{te} m_{te}} \varepsilon_{B,te},$$

as training and test loss for the modified DeepONet. This corresponds to only measuring the branch error, not the full approximation error of the matrix A . This implies

$$\mathcal{L}_{tr} = \frac{1}{nm_{tr}} \sum_{i=1}^N \sigma_i^2 L_{i,tr}, \quad \mathcal{L}_{te} = \frac{1}{nm_{te}} \sum_{i=1}^N \sigma_i^2 l_i.$$

To facilitate the comparison between the unweighted mode losses for test and training data we define the unweighted test loss of mode i as $L_{i,te} = \frac{m_{tr}}{m_{te}} l_i = \frac{m_{tr}}{m_{te}} \|b_{i,te} - w_i\|_2^2$. This implies

$$\mathcal{L}_{te} = \frac{1}{nm_{tr}} \sum_{i=1}^N \sigma_i^2 L_{i,te}.$$

Thus, the unweighted test base loss is $\frac{m_{tr}}{m_{te}} \|w_i\|_2^2$.

H Appendix: Further Optimization Algorithms

H.1 Re-Weighting with Adam

Figure 10 shows the relative error and the weighted mode losses for DeepONets trained using Adam with different exponents e .

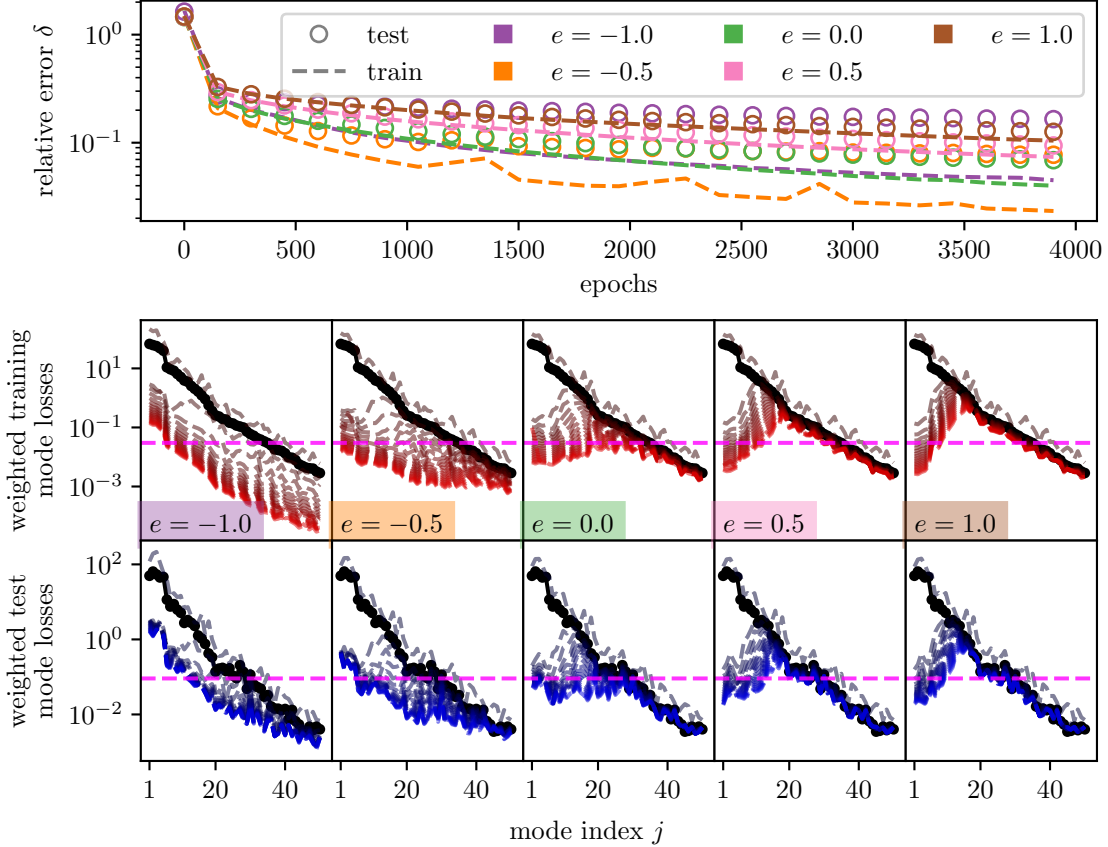


Figure 10: **Model performance across different exponents e and training epochs for modified DeepONets trained using Adam.** Layout and parameters identical to fig. 4, with Adam replacing GD. **Top panel:** Relative error $\delta = \|A - \tilde{A}\|_F / \|A\|_F$ for both training (dashed lines) and test (circles) data across different exponents ($e = -1.0, -0.5, 0.0, 0.5, 1.0$) over 4000 epochs. **Center and bottom row:** Weighted training (center row) and test (bottom row) mode losses at different training steps, colored from gray (initial) to red/blue (final). Each column corresponds to a different exponent e . The third column shows the DeepONet trained using the standard loss ($e = 0$). The center and bottom row plots also contain the respective base losses in black, and a pink dashed horizontal line marking the maximum mode loss in the last training epoch of $e = 0$, facilitating comparison between different exponents e .

H.2 AdaGrad

Figure 11 shows the weighted mode losses for DeepONets trained with GD, Adam and AdaGrad in comparison. We observe that both the overall and the mode specific test loss of the two DeepONets trained with Adam and AdaGrad are very similar.

I Appendix: Spectral Bias

In this section, we provide more information on our spectral bias analysis. The generation of the synthetic data, used in section 6.4.1 to analyze spectral bias in the branch network for data with curated spectral properties, is described in section I.1. The methods to estimate the frequency of the right singular functions for the PDE-derived data is described in section I.2. In section I.2.4 these methods are evaluated on the synthetic data.

I.1 Synthetic Data for Spectral Bias

A prototypical multivariate function $g_k : \mathbb{R}^M \rightarrow \mathbb{R}$ with mean frequency $f = \|k\|_2$ is $g_k(p) = \sin(2\pi k^T p)$. We would ideally set the right singular functions to $\rho_j = g_{f_j z}$ for a family of frequencies $\{f_j\}_{j=1}^N$ and a unit vector $z \in \mathbb{R}^M$, but

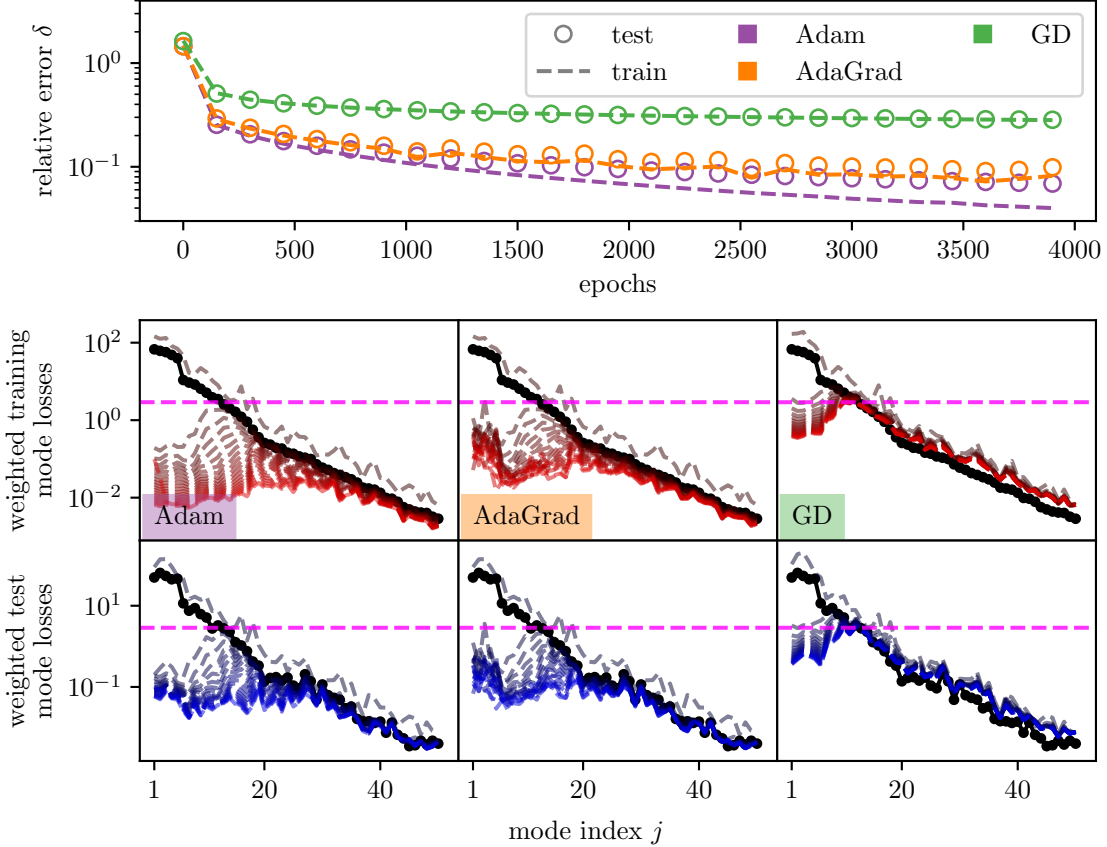


Figure 11: **Model performance for DeepONets trained with different optimizers.** **Top panel:** Relative error $\delta = \|A - \hat{A}\|_F / \|A\|_F$ for both training (dashed lines) and test (circles) data for different optimizers (purple: Adam, orange: AdaGrad, green: GD) over 4000 epochs. **Center and bottom row:** Weighted training (center row) and test (bottom row) mode losses at different training steps, colored from gray (initial) to red/blue (final). The center and bottom row plots also contain the respective base losses in black, and a pink dashed horizontal line marking the maximum mode loss in the last training epoch of the DeepONet trained with GD, facilitating comparison between different algorithms.

the resulting vectors are not necessarily orthogonal. We address this by (1) choosing $p \in \mathbb{R}^M$ and direction vectors such that the resulting vectors are approximately orthogonal, and (2) applying Gram–Schmidt orthogonalization.

Algorithm 1 contains the pseudocode. The algorithm generates m sample points concentrated near the $\mathbf{1}_M = (1 \dots 1)^T$ direction, then constructs a sinusoidal candidate $\sin(2\pi f_j d^T x)$ for each frequency f_j using randomly sampled directions $d \sim \mathcal{N}(\mathbf{1}_M, I_M)$. Candidates are accepted only if their inner product with all previously selected functions is below a threshold of $t = 0.05$, with up to K attempts per frequency. A final Gram–Schmidt step enforces orthogonality of the basis $V = [v_1, \dots, v_N]$. Since there are no truly reliable methods to quantify the frequency of a multivariate function (see section I.2), we estimate the mean frequency of ρ_j to be f_j .

I.2 Frequency Estimation for Multivariate Functions

We seek to characterize the spectrum of $\rho_k : p_j \in \mathbb{R}^M \mapsto V_{jk} \in \mathbb{R}$, which is only available through samples $\rho_k(p_j) = V_{jk}$. Since ρ_k has multi-dimensional input sampled at irregular locations, computing its Fourier transform directly is infeasible [83]. We employ three methods: the total variation (TV) norm [84, 85], the Laplacian energy (LE) [86], and Fourier transforms of projected data [83], described in sections I.2.1 to I.2.3. Both the TV norm and LE rely on a k -nearest neighbors algorithm (k denotes the number of neighbors in this context). For ease of notation, we call the outputs of all methods frequencies, although the TV norm and LE technically compute related quantities.

To compare these methods, we use the relative frequency $f_i / (\max_j f_j)$. Since we are primarily interested in qualitative trends – whether $f(\rho_k)$ increases or decreases with k – rather than exact values, this comparison is meaningful, as

Algorithm 1 Generation of right singular functions with prescribed frequencies

Require: Number of trials K , desired frequencies $F = \{f_1, \dots, f_N\}$, number of samples m , input dimension M
▷ Generate sample points in \mathbb{R}^M

- 1: **for** $i = 1$ to m **do**
- 2: Draw $a \sim \mathcal{U}([0, 1])$ and $b \sim \mathcal{U}([-1, 1]^M)$
- 3: $x_i \leftarrow a(\mathbf{1}_M + 0.1b)$
- 4: **end for**
- 5: $X \leftarrow \{x_i\}_{i=1}^m$
- 6: Set inner-product threshold $t \leftarrow 0.05$
▷ Construct frequency-specific orthogonal functions
- 7: **for** $j = 1$ to N **do**
- 8: **for** $k = 1$ to K **do**
- 9: Draw direction $d \sim \mathcal{N}(\mathbf{1}_M, I_M)$
- 10: Define $w_i \leftarrow \sin(2\pi f_j d^\top x_i)$ for all $i = 1, \dots, m$
- 11: $w \leftarrow [w_1, \dots, w_m]^\top$
- 12: **if** $\max_{1 \leq a < j} |w^\top v_a| < t$ **then**
- 13: $v_j \leftarrow w / \|w\|_2$
- 14: **break**
- 15: **end if**
- 16: **end for**
- 17: **end for**
▷ Final orthogonalization step
- 18: Orthogonalize $\{v_1, v_2, \dots, v_N\}$ using Gram–Schmidt.
- 19: **return** $V = [v_1, v_2, \dots, v_N]$

confirmed empirically in section I.2.4. In the following sections we discuss frequency estimation methods for general functions $g : D \subset \mathbb{R}^d \rightarrow \mathbb{R}$ available through samples $\{x_j, y_j\}_{j=1}^m$ with $y_j = g(x_j)$. Thus, for $g = \rho_k$ we have $x_j = p_j, y_j = V_{jk}$.

I.2.1 Total Variation Norm

The total variation (TV) norm of a differentiable function $g : D \subset \mathbb{R}^d \rightarrow \mathbb{R}$ is $\|g\|_{TV} = \int_D \|\nabla g\|_2 dx$. We approximate it using k -nearest neighbors [87]:

$$\|g\|_{TV} \approx \frac{1}{mk} \sum_{i=1}^m \sum_{j \in N_k(i)} \frac{|y_i - y_j|}{\|x_i - x_j\|_2},$$

where $N_k(i)$ denotes the k nearest neighbors of x_i . This estimates the gradient norm via finite difference quotients between neighboring samples. We use $f(g) = \|g\|_{TV}$ as a proxy for the frequency.

I.2.2 Laplacian Energy

Consider a weighted graph $G = (V, E, w)$ with Laplacian matrix $L \in \mathbb{R}^{v \times v}$ defined by

$$L_{ij} = \begin{cases} -w((i, j)) & \text{if } (i, j) \in E, \\ \sum_{l \in N(i)} w((i, l)) & \text{if } i = j, \\ 0 & \text{else,} \end{cases}$$

where $N(i)$ is the set of adjacent vertices [86]. For undirected graphs, $y^T L y = \sum_{(i,j) \in E} w((i,j))(y_i - y_j)^2 \geq 0$, and the eigenpairs (μ_i, u_i) of L correspond to increasing frequencies with index i .

To apply this to a function g and the samples $\{x_i, y_i\}$, we construct a graph with vertices corresponding to samples and edges from a k -nearest neighbors algorithm. Edge weights are computed via a Gaussian kernel:

$$w((i, j)) = \exp\left(-\frac{k}{2} \frac{\|x_i - x_j\|_2^2}{\sum_{l \in N(i)} \|x_i - x_l\|_2^2}\right).$$

Since the resulting graph is directed, we symmetrize: $L = \frac{1}{2}(L_0 + L_0^T)$. Decomposing any $w \in \mathbb{R}^m$ as $w = \sum_{i=1}^m a_i u_i$ in the orthonormal eigenbasis of L , the Rayleigh quotient

$$\frac{w^T L w}{w^T w} = \frac{\sum_{i=1}^m a_i^2 \mu_i}{\sum_{i=1}^m a_i^2}$$

computes the mean frequency of w as a graph signal. We use the Rayleigh quotient as $f(g)$ for the vector $y = (y_1, \dots, y_m)^T$.

I.2.3 Fourier Transform of Data Projected onto Low-Dimensional Subspaces

Following [83], we project the inputs x_i onto vectors $u_j \in \mathbb{R}^d$ to obtain $a_{ji} = u_j^T x_i \in \mathbb{R}$, defining pseudo functions h_j such that $h_j(a_{ji}) = y_i$. These are “pseudo” functions since the mapping may not be well-defined (e.g., $a_{ji} = a_{jk}$ but $y_i \neq y_k$). We compute their non-uniform discrete Fourier transforms and average over z projection vectors:

$$q(f) = \frac{1}{z} \sum_{j=1}^z \mathcal{F}(h_j)(f), \quad f(g) = \frac{\sum_{f \in F} |q(f)|^2 f}{\sum_{f \in F} |q(f)|^2}.$$

We use the first $z = L$ left-singular vectors of the input data matrix $X = [x_1 \cdots x_m] \in \mathbb{R}^{d \times m}$, which fully reconstruct X since the input functions are sums of L trigonometric functions (see section C). However, the estimated spectrum depends on the choice of projection vectors: different orthonormal sets spanning the same space generally yield different frequency estimates, raising robustness concerns investigated in section I.2.4.

I.2.4 Comparison of Methods

Figure 12 shows the estimated frequencies of the synthetic data using the three methods. The TV norm accurately estimates the true relative frequency, and the LE is qualitatively correct. The projection method fails to capture the trend of increasing frequencies. We tested several projection vector sets (left-singular vectors of X , discrete sine basis), but none reliably captured the frequency trend. We therefore use only the TV norm and LE in section 6.4.1.

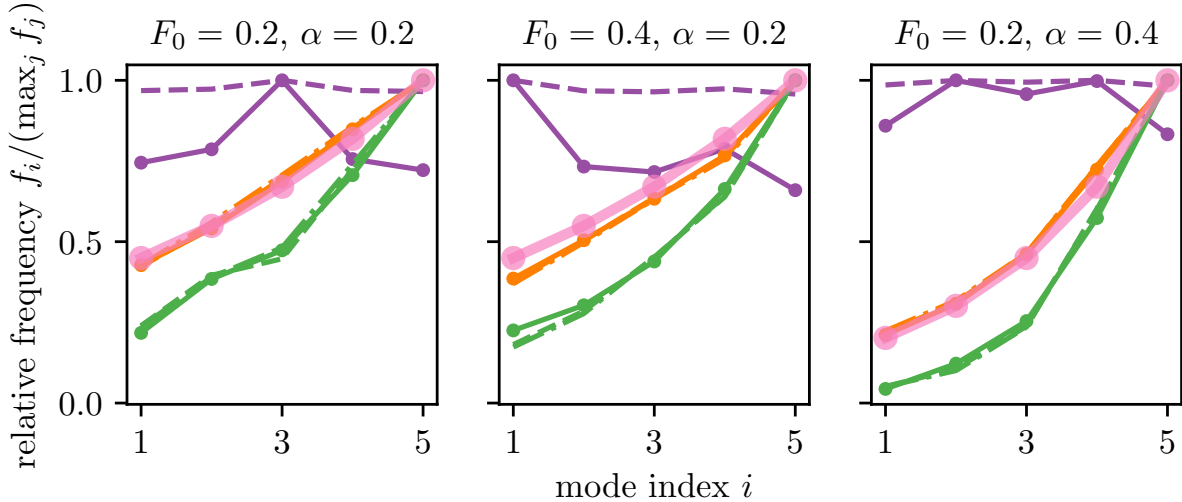


Figure 12: **Estimated frequency of synthetic data.** **Columns:** Different frequency families (synthetic datasets). **Colors and markers:** Pink: Dictated frequency $f_j = F_0 \exp(\alpha j)$, Orange: TV norm (dot-solid: $k = 3$, dashed: $k = 20$, dash-dotted: $k = 50$), Green: LE (dot-solid: $k = 3$, dashed: $k = 50$), Purple: projection (left-singular vectors of X , dot-solid: $k = 1$, dashed: $k = 5$).